JGR Atmospheres

RESEARCH ARTICLE
10.1029/2020JD032947

Key Points:
- Monsoon precipitation consists of diurnal convection and long-duration stratiform systems (LDPS) that determine interannual variability
- The interplay of SA Low-Level Jet and Cold Air Intrusions determines preferred low-level precipitation moisture source regions in the Andes foothills
- LDPS frequency increases when low-level moisture supply is enhanced by midlevel convergence organized by Cold Air Intrusions

Supporting Information:
- Supporting Information S1

Correspondence to:
A. P. Barros,
barros@duke.edu

Citation:
Chavez, S. P., Silva, Y., & Barros, A. P. (2020). High-elevation monsoon precipitation processes in the Central Andes of Peru. *Journal of Geophysical Research: Atmospheres*, *125*, e2020JD032947. https://doi.org/10.1029/2020JD032947

Received 18 APR 2020
Accepted 12 NOV 2020
Accepted article online 23 NOV 2020

Author Contributions:
Conceptualization: S. P. Chavez, A. P. Barros
Data curation: S. P. Chavez
Formal analysis: S. P. Chavez, A. P. Barros
Funding acquisition: Y. Silva
Investigation: S. P. Chavez, A. P. Barros
Methodology: S. P. Chavez
Project administration: Y. Silva
Software: S. P. Chavez
Supervision: A. P. Barros
Validation: S. P. Chavez
Visualization: S. P. Chavez
Writing – original draft: S. P. Chavez
Writing – review & editing: A. P. Barros

High-Elevation Monsoon Precipitation Processes in the Central Andes of Peru

S. P. Chavez[1,2], Y. Silva[2], and A. P. Barros[1]

[1]Department of Civil and Environmental Engineering, Duke University, Durham, NC, USA, [2]Peruvian Geophysical Institute, Ate, Peru

Abstract Measurements at the high-elevation Lamar Observatory in the Mantaro Valley (MV) in the Central Andes of Peru demonstrate a diurnal cycle of precipitation characterized by convective rainfall during the afternoon and nighttime stratiform rainfall with embedded convection. Wet season data (2016–2018) reveal long-duration (6–12 hr) shallow precipitating systems (LDPS) that produced about 17% of monsoon rainfall in 2016 and 2018 associated with El Niño and La Niña, respectively. The LPDS fraction of monsoon rainfall doubles to 35% with weekly recurrence in 2017 under El Niño Costero (coastal) conditions. LDPS occur under favorable moisture conditions dictated by the South America (SA) Low-Level Jet (SALLJ) and Cold Air Intrusions (CAIs). Backward trajectory analysis shows that precipitable water sustains >80% of seasonal precipitation and ties the LPDS to particular moisture source regions in the eastern Andes foothills 1–2 days in advance, enhanced by increased moisture supply in the midtroposphere. Higher frequency of CAIs and enhanced midlevel moisture convergence along CAI fronts explain the increased LDPS frequency during the 2017 El Niño Costero. These findings highlight the functional role of the Andes morphology in organizing moisture supply to high-elevation precipitation systems on the orographic envelope. Analysis of the Global Precipitation Measurement (GPM) mission satellite-based radar observations points to challenges to precipitation detection and estimation in this region as the GPM clutter-free height (~1–2 km AGL) exceeds the depth of shallow precipitation systems in the MV.

1. Introduction

Snow and rainfall in mountainous regions account for half the world's freshwater (Barros, 2013). Orographic precipitation intensity, duration, and seasonality vary from one region to another, reflecting differences in regional climate, topography, and landform (e.g., Barros et al., 2004; Barros & Lettenmaier, 1994; Giovannettone & Barros, 2009). The Central Andes of Peru is the home of 70% of the world's tropical glaciers (Chevallier et al., 2011), and the eastern slopes are a hot spot of biodiversity (Myers et al., 2000). Systematic weather and hydrological monitoring at the temporal and spatial resolution necessary to characterize precipitation processes are lacking, and long historical records are not available yet (Menne et al., 2012; Peterson & Vose, 1997). When precipitation data are available, the measurements consist of daily accumulations from sparsely distributed rain gauges that cannot resolve the diurnal cycle. This limits our understanding of present-day regional hydrometeorology, let alone sensitivity to future climate variability and change. Efforts to overcome these problems rely principally on remote sensing observations and numerical weather prediction (NWP) and or climate model simulations. However, these approaches require validation with in situ observations. For example, in the Central Andes of Peru's foothills, satellite-based precipitation products (e.g., Tropical Rainfall Measurement Mission, TRMM 3B42) can underestimate annual rainfall up to 300% on average (Lowman & Barros, 2014). Whereas new products (e.g., IMERG; Huffman et al., 2015) using Global Precipitation Mission (GPM) observations show substantial improvements over the TRMM era, significant underestimation errors in mountainous regions tied to ground clutter artifacts remain (Barros & Arulraj, 2020).

On the Andes' eastern slopes, the steep and tortuous 3-D topography results in strong precipitation gradients and complex spatial patterns of precipitation (Nesbitt & Anders, 2009; Biasutti et al., 2012; Chavez & Takahashi, 2017, hereafter CT17). The Central Andes of Peru encompasses mountain ridges above 6,000 m ASL (above sea level), canyons of 3,000 m depth, myriad valleys, and the Amazon rainforest at lower elevations. Along with the Andes-Amazon transition, the low-level moisture flux (MF) coming from the Amazon is blocked by the mountains and turns southward out of the tropics of South America (Campetella & Vera, 2002; Marengo et al., 2004; Salio et al., 2002; Vera et al., 2006). Enhanced

10.1029/2020JD032947

convergence along the Andes' foothills produces heavy rainfall resulting in three well-defined precipitation hot spots (i.e., regions where the mean annual rain is at least double the mean rainfall in the Amazon region; Espinoza et al., 2015; CT17). Heavy orographic precipitation in the central Andes has also been linked to southerly cold fronts that originate in the midlatitudes in South America (Cold Air Intrusions, CAIs) and latch to the eastern slopes of the Andes in their northward progression (Eghdami & Barros, 2019).

The spatial distribution of regional orographic precipitation is associated with favorable large-scale moisture transport and the interaction between precipitation systems (PSs) and topography (Giovannettone & Barros, 2009; Romatschke & Houze, 2010). In the eastern foothills of the central Andes, abundant moisture carried by the South American Low-Level Jet (SALLJ) permits the development of mesoscale convective systems (MCSs; Liu, 2011; Rasmussen et al., 2016; CT17). Dry conditions inhibit the MCS development at high elevations (above 3,000 m ASL; Mohr et al., 2014). Valley systems such as the Apurimac River Valley System (14°S) channelize the MF from the foothills of the Andes to the highlands (Junquas et al., 2018; Killeen et al., 2007). However, the reliability of this upslope moisture transport depends on moisture convergence along the foothills and low-level moist entropy. The latter is closely tied to the modulation of atmospheric stability by evapotranspiration from tropical montane forests in the foothills of the Andes (Eghdami & Barros, 2020; Sun & Barros, 2015a, 2015b).

Based on the TRMM precipitation radar (PR) product 2A25 and the rain gauges from the Servicio Nacional de Meteorologia e Hidrologia of Peru (SENAMHI), the rainiest region of Peru is between Cusco and Madre de Dios (Biasutti et al., 2012; Espinoza et al., 2015; Nesbitt & Anders, 2009; CT17). Large systems produce this precipitation, and 86% of these systems prevailing for strong SALLJ conditions. In contrast, the remainder PSs (14%) are linked to CAI activity (CT17). Eghdami and Barros (2019) analyzed rain gauge data, TRMM precipitation features (PFs; Liu et al., 2008), and European Center for Medium-Range Weather Forecasts (ECMWF) Reanalysis (ERA-Interim) data to investigate orographic rainfall extremes in the eastern slopes of the central Andes. They found that during CAIs, moisture convergence at higher elevations (above 3,500 m) is significantly larger than on days of average and more vigorous SALLJ conditions (CT17; Eghdami & Barros, 2019). Indeed, at the Quelccaya glacier, located next to the hot spot of precipitation in the central Andes, snow records analysis indicates that CAIs are responsible for most of the snow accumulation (Hurley et al., 2015).

At locations in the inner mountain region, solar forcing and local circulations strongly influence precipitation's diurnal cycle. In the valleys of the central Andes and at low elevations and the base of the in the Apurimac River Valley System (13.5°S, 74°W), most of the rainfall is observed during the night and early morning (CT17; Giovannettone & Barros, 2009; Junquas et al., 2018). At high elevation in Cusco (13.5°S, 71.9°W), afternoon short-duration convective cells produce heavy precipitation, and longer duration stratiform PSs predominate at night (Endries et al., 2018; Perry et al., 2017). Nevertheless, in the western highlands of the central Andes of Peru, most of the rainfall is observed in the afternoon (CT17; Mohr et al., 2014). High-resolution simulations in the Apurimac River Valley System (Junquas et al., 2018) show that daytime upslope valley winds carry moisture to the surrounding ridges with a reversal at night independent of valley orientation on the orographic envelope. Lowman and Barros (2014) showed that the centroids of TRMM PFs in the central Andes are in the ridges between 1 and 7 p.m. LT (local time) and in the valleys between 1 and 7 a.m. LT.

Interannual variability of precipitation in the Peruvian Andes has long been linked to variability in ENSO activity. Takahashi et al. (2011) proposed two indices of sea surface temperature (SST) anomalies tied to ENSO based on eastern Pacific (E) and central Pacific (C) conditions. Subsequent studies found that positive/negative C conditions are associated with dry/wet anomalies in the Central Andes of Peru. In contrast, positive E conditions are associated with the southern displacement of the Intertropical Convergence Zone (ITCZ) and therefore more rainfall in northern Peru (Lavado-Casimiro & Espinoza, 2014; Sulca et al., 2018). Both indices are associated with westerly wind anomalies that generate less than average rainfall and negative mass balance in glaciers in the tropical Andes (Francou et al., 2004; Vuille et al., 2008). However, the E index's significant anomalies are restricted to the south of Peru (Sulca et al., 2018). El Niño activity was highly variable in 2016–2018. The Strong El Niño in 2016 with low precipitation across Peru was followed by the El Niño Costero (coastal; Takahashi & Martínez, 2019) in January–March (JFM) of 2017 that caused extensive flooding in north-central coastal Peru and widespread landslides in the inter-Andean Valleys (Ramírez & Briones, 2017), and a moderate La Niña in 2018.

10.1029/2020JD032947

The meteorology of high-elevation monsoon rainfall in the central Andes has been studied at the event-scale and selected locations (e.g., Flores et al., 2019; Martínez-Castro et al., 2019; Moya-Álvarez et al., 2018). In this study, the region of interest is the Mantaro Valley (MV; Figure 1) that is nestled in the central Andes with a north-south orientation and a mean elevation of 3,300 m. The MV's eastern (Amazonian) flank is the Huaytapallana chain that reaches 5,500 m ASL elevation. The Huaytapallana glacier (HG) is a crucial freshwater source in the dry season. Agriculture and water resources in the MV provide essential food supplies and hydroelectricity to Lima, Peru's capital city, where around 10 million people live. Heightened concerns with water resources in the MV stem from the recent acceleration of the HG retreat due to global warming (e.g., Rabatel et al., 2017; Vuille et al., 2008). Furthermore, the MV is highly vulnerable to extreme hydrological events, including floods, frosts, and landslides that threaten agriculture (Espinoza et al., 2013; Lavado Casimiro et al., 2010; Saavedra & Takahashi, 2017; Zubieta et al., 2017). Understanding the dynamics of precipitation in this valley is key to regional water security and socioeconomic resilience.

The Laboratory of Atmospheric Microphysics and Radiation (LAMAR) of the Peruvian Geophysical Institute (IGP) is a measurement site that has been operational since 2015 (Figure 1). LAMAR is equipped with a Ka-band vertical profiling radar, an optical disdrometer, two rain gauges, and a vertical profiler wind radar (Table 1). These instruments measure the vertical structure of clouds and precipitating systems for the first time in this region, the rain type, the drop size distribution, and the low-level and midlevel winds. LAMAR observations enable examining the diurnal cycle of precipitation that is key to understand regional precipitation processes and provide ground-validation for remotely sensed precipitation products. LAMAR data provide information on the temporal structure of surface precipitation at point scale; TRMM and GPM data provide information on spatial structure and the diurnal cycle climatology at a regional scale. The objective of this study is to characterize the diurnal cycle and interannual variability of monsoon precipitation at high elevation in the Central Andes of Peru using the ground-based LAMAR data and long-term satellite-based remotely sensed precipitation products from the TRMM and the Global Precipitation Measurement (GPM) mission.

The manuscript is organized as follows. Sections 2 and 3 describe the data and data-analysis methods, respectively. Results are presented in section 4, which is organized to highlight the diurnal cycle of precipitation structure and interannual variability of precipitation in the context of regional hydrometeorology. In section 4.1, the focus is on the diurnal cycle of rainfall, including the vertical structure of PSs and the associated microstructure of surface rainfall (i.e., the raindrop size distribution, DSD) from ground observations and vertical and horizontal structure (i.e., spatial PFs) from satellite observations. In section 4.2, the focus is on elucidating the synoptic precursors of long-duration precipitation systems (LDPS) toward explaining LDPS frequency changes that account for significant interannual variability of MV monsoon precipitation (~30%). The manuscript concludes in section 5 with a synthesis of results, discussion of findings, and future work outlook.

2. Data

2.1. Ground Observations

Table 1 provides a detailed list of the suite of instruments at the LAMAR observatory, including characteristics of the measurements used in this work. The data are publicly available from Duke University Repositories.

Rain gauge data at 1 min temporal resolution from January 2016 to March 2018 were used to calculate rain rate and accumulation. DSDs from an optical disdrometer (e.g., Parsivel-2) at 1 min temporal resolution were available from September 2017 to March 2018.

Three monsoon seasons of reflectivity data from the Doppler pulsed 35 GHz Ka-band vertical profiler radar (JFM 2016, December–February [DJF] 2017, and JFM 2018) were available for analysis. An attenuation correction algorithm is not available for the LAMAR Ka-band radar. Rain rates exceeding 5 mm/hr are not frequent at LAMAR even at the monsoon season's peak. However, attenuation errors can be severe for convective precipitation. Rain gauge and disdrometer measurements are used to identify attenuation artifacts that might lead to misclassifying precipitation type (stratiform or convective) from ground-based radar observations.

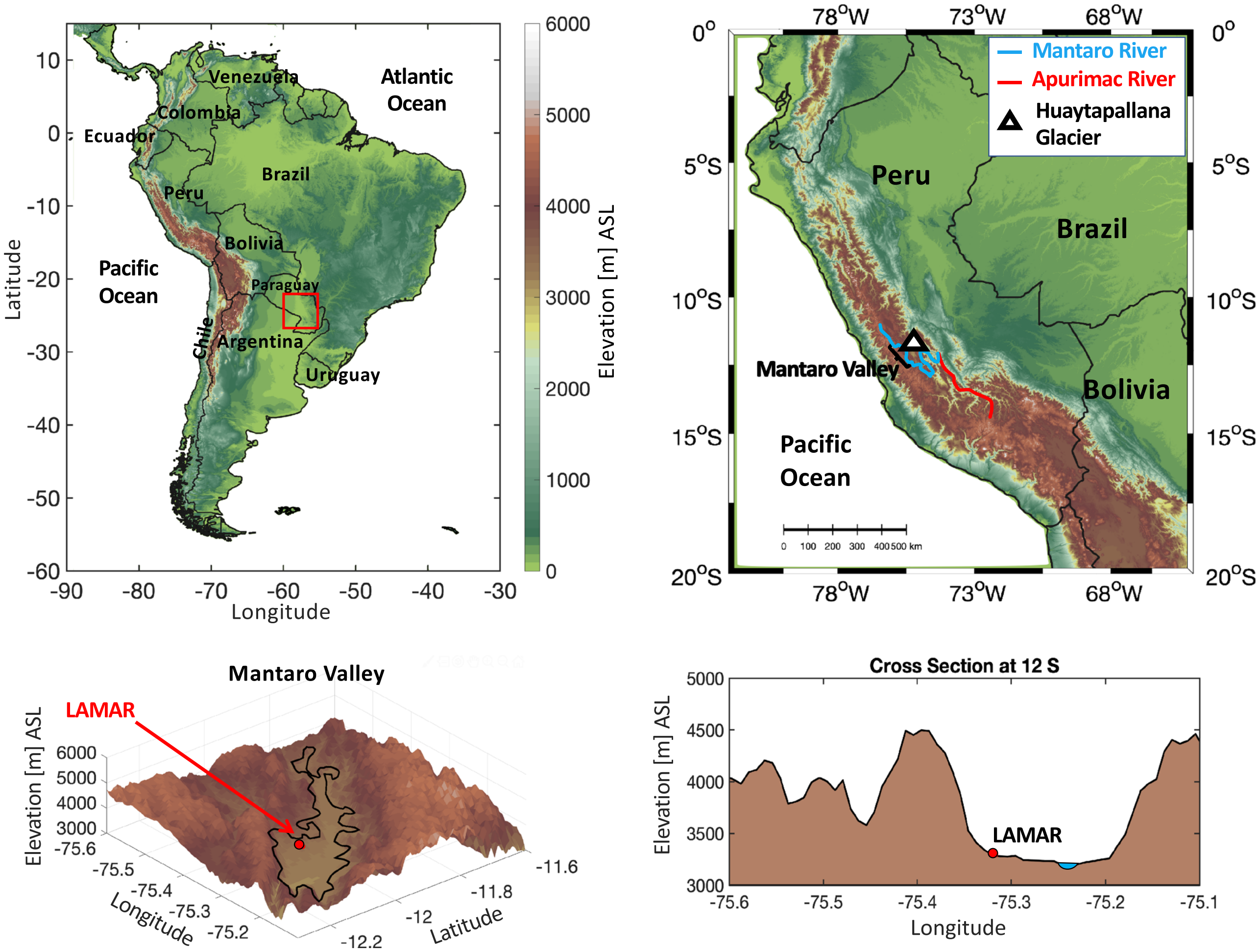

Figure 1. Top left: map of terrain elevation of South America; the red square is the region used to detect Day 0 cold air incursions. Top right: map of Peru showing the Mantaro and Apurimac rivers and the location of the Mantaro Valley (MV). Bottom left: 3-D digital elevation model of the MV. Bottom right: cross section at 12°S of the MV. The red dot marks the location of the Laboratory of Atmospheric Microphysics and Radiation (LAMAR).

Vertical profiles of wind velocity for each component *u*, *v*, and *w* were obtained from the Boundary Layer Tropospheric Wind Radar (BLTR) during JFM 2016 and DJF 2017. The BLTR radar operates at 50 MHz and is sensitive to rainfall and winds. Thus, its utility is merely qualitative for assessing winds during rainfall.

Table 1
Overview of Sensor Characteristics at LAMAR

Sensor	Variable	Units	Accuracy	Samp. Rate	Period	References
Tipping Bucket Rain Gauge	rainfall	mm	0.254 mm	1 min	01/2016 to 03/2018	www.onsetcomp.com/files/manual_pdfs/10241-D-MAN-RG3.pdf
Optical Disdrometer Parsivel 2 OTT	radar reflectivity factor Drop Size Distribution (N(D))	dBZ log10 $(1/m^3\ mm)$	Range: [−9, 99] Range: [0.05, 27.5 mm]	1 min	09/2017 to 03/2018	//www.otthydromet.com/en/p-ott-parsivel
Ka-band cloud radar Mira35c	radar reflectivity factor	$mm^6\ m^{-3}$ and dBZ	Sensitivity: −40 dBZ No attenuation correction	5.3 s	01/2016 to 02/2017 01/2018 to 03/2018	//http://metek.de/product/mira-35c/#
Boundary-Layer Tropospheric radar	wind components *u*, *v*, and *w*	$m\ s^{-1}$	~0.1 $m\ s^{-1}$	1 min	01/2016 to 03/2016 and 12/2016 to 02/2017	DOI: 10.13140/RG.2.2.30331.26404

2.2. Satellite Observations

TRMM PR swath products 2A23 and 2A25 Version 7 (Awaka et al., 2009; Iguchi et al., 2009; Iguchi, Meneghini, et al., 2000; Kozu et al., 2009) over 15 years (1 January 1998 to 31 December 2012) were used to extract PFs and the climatology of precipitating systems echo-top heights. GPM dual precipitation radar (DPR) product 2ADPR Version 06 with Normal Scan (NS) swaths (Iguchi et al., 2017) starting on 1 November 2014 through 31 March 2020 are used for the same purpose as the TRMM PR data. GPM-DPR Ku-band NS swaths are used to determine the ground clutter-free height (i.e., the height above which reflectivity measurements are not contaminated by ground backscatter).

There are critical differences in the sensitivity of the GPM KuPR and the TRMM PR, as well as in measurement errors—for example, sidelobe clutter contamination for the Ku-PR (Kubota et al., 2016) and ground clutter (Iguchi et al., 2017)—and in viewing geometry (e.g., parallax errors; Hamada & Takayabu, 2016). Caution in integration and interpretation of GPM and TRMM measurements is therefore warranted. Besides, an optimization approach based on a relationship between rain rate and mass-weighted diameter was implemented in Version 6 of the DPR algorithm (Liao & Meneghini, 2019) in contrast with the TRMM PR single-wavelength algorithm (Iguchi et al., 2009; Iguchi, Meneghini, et al., 2000). Overall, deeper profiles and more extensive PFs are expected from DPR due to improved light rainfall detection.

2.3. Reanalysis

The ERA-Interim (Dee et al., 2011) at 0.75° × 0.75° horizontal resolution and 6 hr time steps was used as the meteorological input for trajectory analysis using the Hysplit model (Stein et al., 2015). ERA-Interim was used for back trajectory analysis on the orographic envelope to identify moisture source regions. ERA Version 5 (ERA5; Hersbach et al., 2020) at 31 km spatial resolution and hourly time steps was used to probe interannual variability of moisture sources. In particular, we used the hourly pressure levels fields of winds (u, v) and specific humidity (q) during January 2000–2019 and during January and February of 2016–2018.

3. Data Analysis Methodology

3.1. Ground Observations

3.1.1. Reflectivity Profiles

First, vertical reflectivity profiles from the Ka-band radar at the original temporal resolution of 5.3 s were averaged to 10 min. Second, the diurnal cycle of vertical reflectivity structure under rainy conditions was derived from profiles where the near-surface reflectivity (280 m AGL, above ground level) is greater than 0 dBZ. This threshold is an indicator of light rainfall based on the disdrometer and rain gauge observations at LAMAR. The vertical structures of the Ka-band reflectivity profiles for the three wet seasons 2016–2018 were summarized in a contoured frequency by altitude diagram (CFAD) to display the relative occurrence of radar reflectivity as a function of height. The relative occurrences were obtained by counting the reflectivity values above the minimum threshold of −20 dBZ for each bin (31 m height) at one dBZ intervals.

3.1.2. Wind Profiles

Raw BLTR wind profiles were averaged to 10 min resolution. Profiles of each wind component concurrent with Ka-band near-surface reflectivity greater than 0 dBZ were extracted to derive the diurnal cycle when rainfall is measured at the surface.

3.1.3. Precipitation Systems

PSs were classified based on duration and vertical precipitation structure as they passed over the ground-based Ka-band radar during JFM of 2016, DJF of 2017, and JFM of 2018 when complete observational records are available at LAMAR. Note that the Ka-band radar data are 2-D; that is, the vertical axis is the range, and the horizontal axis is time. The PSs were extracted from the 10 min average reflectivity profiles time series as follows. First, the contiguous areas where reflectivity is higher than −15 dBZ are identified. This low threshold accounts for radar attenuation and cloudiness while reducing fragmentation of persistent PSs, and it is suitable for detecting embedded convection systems. Only PSs with at least one value of reflectivity higher than 20 dBZ near the surface were submitted to further analysis to eliminate cloud systems with no precipitation or very light precipitation. Next, the shape of each PS is delineated by fitting an ellipse to its area. The centroid of the ellipse and the minor and major axes serve as PS metrics. Because of the alignment of the PSs in range-time space, the principal (vertical) axis represents the PS range or height AGL, and the minor (horizontal) axis represents the PS duration in minutes. Finally, the PSs were categorized as long-duration PSs (LDPSs) if rainfall lasts at least 6 hr according to the Ka-band radar, disdrometer, and rain gauge observations. All other PSs lasting less than 6 hr are considered short-duration PSs. A precipitating system is classified as shallow precipitation if it has no reflectivity above 20 dBZ above the isotherm of 0° (around 5,000 ASL or 1,700 AGL).

3.1.4. Rain Microphysics

The DSD is expressed as the number of drops per volume of air for a given drop size interval refereed as N(D) (Tokay et al., 2014). The DSDs' hourly diurnal cycle was calculated by averaging 1 min N(D) measurements when hydrometeors were detected. Hourly totals of detection counts (detection counts for a given drop size interval per minute) were also calculated. The contrast between DSD diurnal cycles in the austral spring (September–November, SON) and in the summer monsoon (DJF) highlights seasonal changes in the type of PSs.

3.1.5. Rain Gauge Accumulations

The diurnal cycle of hourly monsoon rainfall was obtained by accumulating separately the hourly totals for LDPS and short-duration PS categories during January and February of 2016, 2017, and 2018 for consistency with other data sets.

3.2. Satellite Observations

3.2.1. Echo-Top Heights

Andes-Amazon transects of echo-top heights from TRMM PR reflectivity measurements for the 1998–2012 period and from GPM DPR Ku-band for 2014–2020 were obtained following CT17. These transects are centered in the 1,000 m ASL topographic contour over ~3.5° latitude from 10° to 13.5°S. The vertical distribution of echo-top heights was calculated by counting all echo-tops heights in bins of 200 m elevation for 6 hr intervals. Only observations in the center part of the DPR Ku swath (four rays at each side of the nadir ray, nine rays in total) are used to minimize sidelobe clutter and parallax errors.

3.2.2. Clutter-Free Heights

The GPM DPR clutter-free height was calculated for Ku-band NS mode over the period March 2014 to March 2019 using as reference the GPM-DPR Level 2 algorithm theoretical basis document (Iguchi, 2018).

3.2.3. Precipitation Features

TRMM PR PFs are rainy areas of contiguous pixels with an estimated surface rain rate greater than 0.15 mm/hr, according to Romatschke and Houze (2013). PFs' horizontal extend was identified from the TRMM PR 2A25 instantaneous swath product (Iguchi, Kozu, et al., 2000) and the precipitation type (convective or stratiform) from the TRMM 2A23 product (Awaka et al., 2009; Funk et al., 2013). The PFs were categorized by horizontal area in three categories small (S, 25–2,250 km^2), medium (M, 2250–24,700 km^2), and large (L, >24,700 km^2). GPM DPR Ku-band NS swaths were analyzed to extract PFs over the MV in the 2014–2020 period. Analogous to TRMM-PR PFs, the GPM-DPR PFs were organized by their horizontal area in S, M, or L. Then, after the size of the PFs is determined, pixels within the MV are identified. The precipitation type (convective and stratiform) and the rain intensity were used to calculate the rain-type contribution for MV pixels only. This approach allows us to determine the rain contribution by type (convective and stratiform) of S, M, and L size PFs to the MV.

3.3. Reanalysis

3.3.1. Moisture Transport

Moisture transport was mapped by following the back wind trajectories (HYSPLIT; Stein et al., 2015) starting 500 m AGL in the MV at 13 LT in the afternoon over the previous 48 hr every 6 hr from January to February in 2016–2018. Subsequently, trajectories were divided into two subgroups corresponding to LDPS and short-duration PS days. On any given day, the analysis gives precedence to LDPSs because they start in the afternoon or the evening and last until the morning of the next day, thus dominating daily rainfall when they occur. There is one case only when the LDPS begins at 08:00 LT and lasts until 23:50 LT.

3.3.1. Moisture Flux and Moisture Flux Convergence

ERA5 hourly specific humidity (q) and horizontal winds $\overrightarrow{V_h} = (u, v)$ were used to obtain the horizontal MF (MF $= q\ \overrightarrow{V_h}$) and daily values were used to obtain moisture flux convergence (MFC; MFC $= -\ q\nabla.\overrightarrow{V_h}$) at different pressure levels. Cross sections of the zonal MF (west-east, qu) at 12°S were averaged to monthly values for January and February in 2016–2018. Daily averages of q, $\overrightarrow{V_h}$, MF, and MFC were obtained for

10.1029/2020JD032947

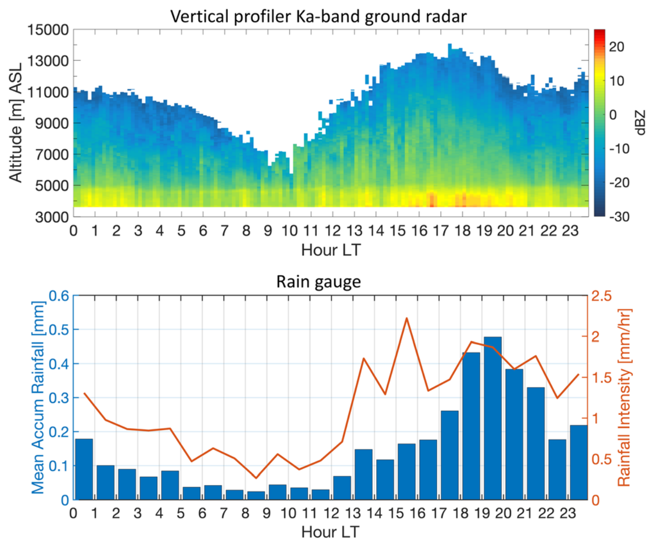

Figure 2. Top panel: diurnal cycle of Ka-band radar reflectivity concurrent with surface rainfall during the three wet seasons JFM of 2016, DFJ of 2017, and JFM of 2018 at the LAMAR site located in the Mantaro Valley (Figure 1). Bottom panel: mean hourly rainfall accumulations (blue bars) and rainfall intensity, that is, the mean hourly rainfall without zeros (orange line) from the Lamar rain gauge during JFM of 2016, DFJ of 2017, and JFM of 2018.

the day of LDPS detection (Day 0) and the past 48 hr (Days -1 and -2). A 20 year (2000–2019) climatology of January MF was derived from the hourly fields.

4. Results and Discussion

4.1. Diurnal Cycle of Precipitation

4.1.1. Ground Observations

4.1.1.1. Vertical Structure

The reflectivity profiles of precipitating systems in the MV reveal a robust diurnal cycle (Figure 2) with precipitation occurring mostly in the afternoon and at night and very low accumulations from early morning (5 a.m. LT) to early afternoon (12 LT). The corresponding wind profiles provide qualitative insight into the underlying processes (Figure S1 in the supporting information). In the afternoon, in particular, between 16 and 20 LT, the reflectivity profiles reach altitudes above 11,000 ASL despite attenuation. The wind profiles show upward vertical motion in the lower 1 km consistent with convective activity forced by solar heating, as suggested by previous studies (Martínez-Castro et al., 2019; Moya-Álvarez et al., 2018). Vertical motion is downward or negligible at other times at all elevations. Because wind and raindrops velocities are averaged together in the BLTR profiles, it is impossible to determine wind direction conclusively during rainfall. Nighttime rainfall intensities (20–07 LT) are lower than during the afternoon. Reflectivity profiles exhibit a bright-band feature (local reflectivity peak) below 5 km ASL typical of stratiform precipitation (Houze, 2014). Besides, there are some intervals in the early morning with no bright band and no downdraft but localized updrafts instead (Figure S1), suggesting stratiform precipitation with embedded convection.

A synthesis of the vertical structure of precipitation based on the Ka-band reflectivity profiles is presented in Figure 3. On average, the 0° isotherm is at 5,000 m ASL (~1,700 m AGL) as shown by the bright-band between 4,700 and 5,000 m ASL (1,400 and 1,700 m AGL) due to hydrometeor melting below the 0° isotherm. The flattening of the low-frequency contours for reflectivity above 20 dBZ illustrates the impact of attenuation for heavy (convective) precipitation.

Figure 4 (right column) shows the diurnal cycle of rain DSDs during the 2018 monsoon (JFM) and the DSD diurnal cycle in the previous spring (SON; Figure 4, left column) for contrast. The DSD diurnal cycle is depicted in terms of counts (number of detections for a given drop size interval per minute, top row) and drop number concentration N(D), which is the number of drops per volume of air for a given drop size interval.

In the summer months, that is, JFM of 2018, large counts are observed at all times compared to the spring (SON), except around noon. In particular, large drops with diameters greater than 1.75 mm are measured between 15 and 21 LT and in the early morning (2–6 LT). The latter is concurrent with the peak in rainfall produced by LDPSs at that time (Figure 4, right panel). The large differences between JFM and SON are in the magnitude of the spike in detections associated with convective rainfall in the late afternoon and into the evening (18–21 LT), and in summer nighttime detections (21–06 LT) tied to LDPSs in contrast with negligible counts in the spring. Drops with diameters larger than 2.00 mm are observed during convective rainfall episodes (15–21 LT), and diameters as large as 4.0 mm can be detected in the late afternoon, albeit infrequently. Rare large drops (diameter >4.5 mm) are likely associated with melted graupel or hail during the afternoon. Drop diameters remain below 2 mm at nighttime (21–06 LT) with substantive drop number concentrations N(D) during the monsoon consistent with persistent light rainfall (Figure 2).

Drop-counting errors in optical disdrometers are large for very small drops due to instrument accuracy limitations. This is in part due to instrument sensitivity (drops smaller than ~0.2 mm effectively cannot be measured), drop overlap when concentrations are very high resulting in large undercount errors, and wind conditions that strongly impact drop trajectories and deviate drops from the measurement volume

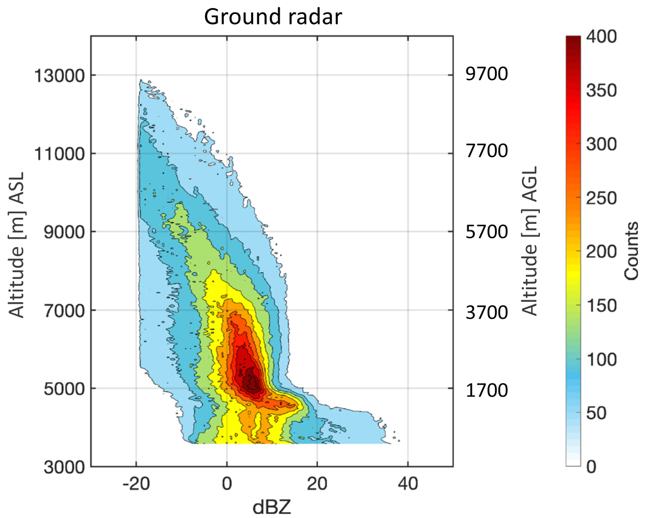

Figure 3. Ground-based Ka-band radar reflectivity CFAD for January–March and December of 2016, January–February of 2017, and January–March of 2018. The shading scale represents the number of counts in bins of 31 m altitude and one dBZ reflectivity.

(e.g., Angulo-Martinez & Barros, 2015; Testik et al., 2006). Nevertheless, the late-night (0–3 LT) monsoon peak in detection counts and the light rainfall and large drop counts at midday in both spring and summer (Figure 4) also resemble disdrometer observations in the Southern Appalachian Mountains attributed to seeder-feeder interactions (SFIs) between stratiform precipitation aloft and low level clouds and fog (Duan & Barros, 2017; Wilson & Barros, 2014, 2015). Additional measurements, in particular, high-resolution reflectivity profiles obtained from low-frequency radars to reduce attenuation would be necessary to be conclusive.

4.1.1.2. Precipitation Systems

Two types of PSs were identified according to rainfall duration and intensity using the concurrent disdrometer, rain gauge, and Ka-band radar measurements following the methodology described in section 3.1: (1) short-duration (<6 hr) PSs that are the most frequent type and (2) infrequent LDPS. Only 11 LDPS were detected during the study period.

Figure 5 shows the temporal evolution of reflectivity (top row) and drop size distribution (bottom row) for an afternoon short-duration PS (duration <3.5 hr) and a nocturnal LDPS (duration >8 hr). The microphysics of short-duration PSs exhibits the signature of vigorous convection, including large raindrops (drop diameters up to 4 mm) in the late afternoon and high reflectivity (40 dBZ), the vertical extent of which is impacted by severe attenuation between 18:30 and 19:30 LT. Note the

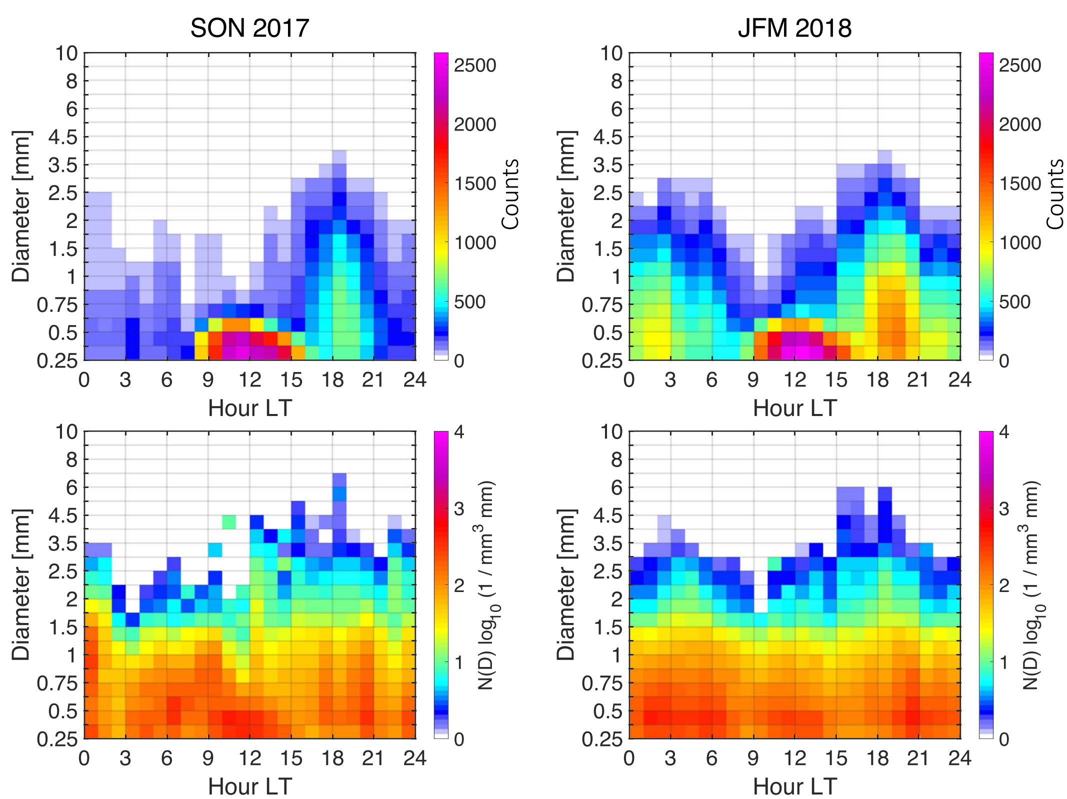

Figure 4. Diurnal cycle of the drop size distribution from measurements of the optical disdrometer Parsivel 2 at 1 min time scale. Left: September–November (SON) of 2017. Right: January–March (JFM) 2018. The *x* axis is the hours of the day. The *y* axis is the drop diameter. The color scale represents the number of detections (top row) and N(D) (bottom row).

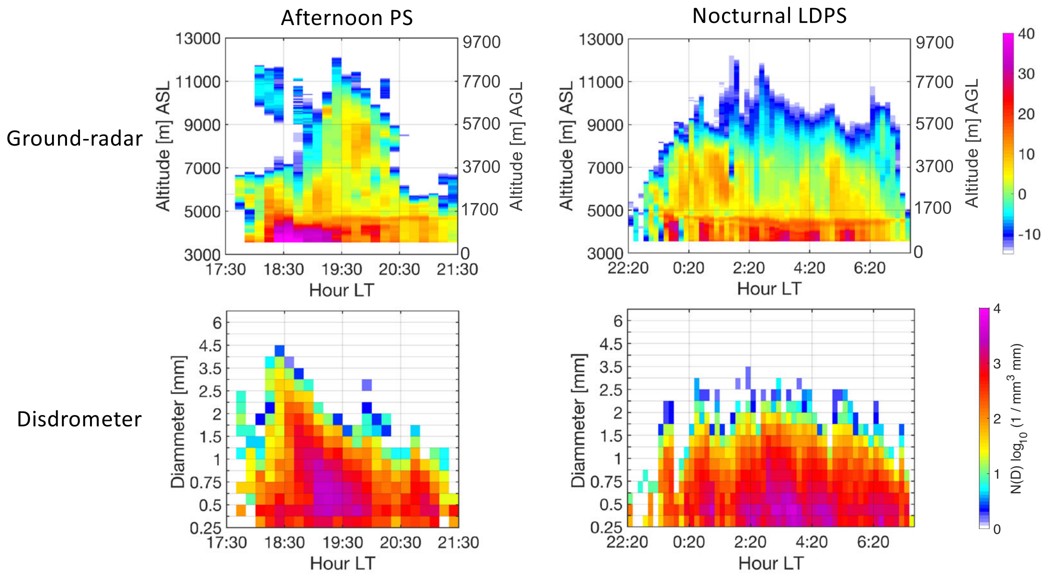

Figure 5. Ka-band reflectivity vertical profiles (top row) and disdrometer raindrops number concentration N(D) (bottom row) for a short-duration PS in the late afternoon (left column) and a nocturnal LDPS (right column).

deep clouds up to 9 km between 19:30 and 20:30 LT as the PS microphysics evolve into light rainfall (drop diameters less than 1 mm). The LDPSs show persistent stratiform rainfall characteristics, including the presence of a bright band, drop diameters ≤2 mm, and echo-top heights (using a 0 dBZ threshold) in the 7–8 km range. Episodic increases in reflectivity synchronous with large increases in small drop number concentrations past midnight (2–6 AM LT) suggest the possibility of SFI among layered clouds, including melted ice hydrometeors and near-surface radiation fog not unlike those reported by Wilson and Barros (2014). Intermittent high reflectivity (>30 dBZ) is attributed to short-lived embedded convection initiated by the forced lifting of warm moist valley air at the katabatic front associated with drainage winds from surrounding ridges.

The mean vertical structure of short duration PSs at different times of the day is shown alongside nocturnal LDPSs in Figure 6 for the 3 years when ground-based radar data are available. Short-duration PSs were assigned to the 6-hr interval where they spend more time. Note that the Ka-band radar detects not only the precipitating regions but also the associated clouds. The left panel in Figure 6 shows that the depth of short duration PSs generally does not exceed 4 km, although the full vertical development of some PSs can reach heights of 12 km ASL (8.7 km AGL). LDPSs exhibit a much higher frequency of deep clouds in the 8–10 km ASL (4–6 km AGL) range compared to all other PSs except in the afternoon (15–20 LT) due to convective activity.

Using a threshold of 0 dBZ to identify echo-top heights shows that shallow precipitation is predominant (~3.5 AGL and ~7 km ASL), although occasionally deep PSs extend up to 12–14 km ASL (right panel). Because the LDPSs nocturnal echo-top heights are above 5 km more than 50% of the time, there is an important contribution from midlevel stratiform precipitation to the observed rainfall rates at the surface consistent with the ubiquitous bright-band in the time series of reflectivity. Falling ice hydrometeors melt below the 0° isotherm and seed warm low-level clouds explaining moderate rainfall rates (3–5 mm/hr; Figure S2) concurrent with large numbers of small drops amidst a background of light rainfall (2:20–4:20 LT in Figure 5, right column).

4.1.2. Satellite Observations

4.1.2.1. Vertical Structure

The distribution of echo-top height measurements along transects between 10°S and 13.5°S reveals the diurnal cycle of echo top heights of precipitating systems in the transition region from the Andes Mountains to the Amazon (Figure 7a for TRMM; Figure 7b for GPM).

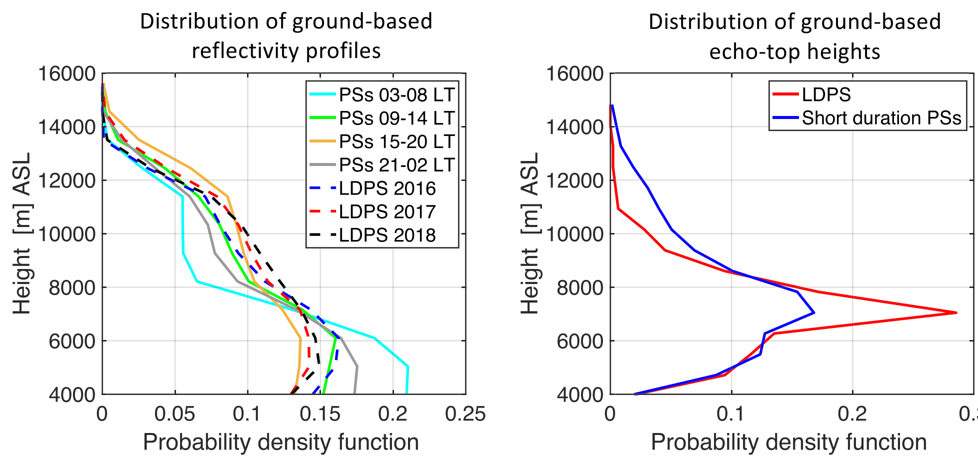

Figure 6. Left: probability density function of ground-based Ka-band radar reflectivity profiles (greater than −15 dBz) of short-duration PSs at different times of day (continuous lines) and for nocturnal LDPSs in different years (dashed lines) at LAMAR. Right: probability density function of the Ka-band radar echo-top heights (0 dBZ threshold) of short duration PSs (blue line) and for nocturnal LDPSs (red line) at LAMAR. Radar data are available for January–March and December of 2016, January–February of 2017, and January–March of 2018.

In the context of Figure 7, the Andes mountains refer to the region where the average terrain elevation is above 2,000 m ASL, and the average terrain elevation is between 500 and 2,000 m ASL in the Andes foothills. Generally, echo tops in the Andes Mountains during the afternoon (13–18 LT) are higher (5–13 km) than in the foothills (5–9 km). At LAMAR in particular (black dashed line in Figure 7), the TRMM PR echo-top heights (Figure 7a) range from 5,500 to 12,500 m in agreement with the Ka-band radar (Figures 2 and 3). In the evening and at night (19–00 LT), the number of echo-top heights between 5 and 9 km altitude diminishes in the foothills toward the Amazon, and echo-tops above 10 km are not detected over the mountains. In the early morning (01–06 LT), echo-tops heights over the foothills reach their daily maximum altitude. This behavior was also reported by CT17, who showed convective systems having greater depth and higher rain rate in the Andes-Amazon transition region at that time. Nocturnal mountain downslope winds interacting with the warm moist flow from the Amazon basin along the Andes foothills as proposed by Giovannettone and Barros (2009) can explain the alignment of nocturnal convective activity at low elevations against the foothills apparent from infrared imagery and the diurnal cycle of TRMM precipitation (Liu et al., 2008; Lowman & Barros, 2014).

The TRMM echo-top heights in the early morning at LAMAR range from 5–8 km in agreement with the Ka-Band radar measurements, but the frequency is much lower than elsewhere in the region at any time. Fewer echo tops occur over the Andes and the foothills in the morning (7–12 LT) as precipitating systems decay from convective to stratiform (CT17).

The distribution of GPM DPR Ku-band echo-top heights is shown in Figure 7b. Besides the differences in the record length compared to TRMM, the much lower counts for GPM also reflect comparatively few overpasses at low latitudes when it is raining and the fact that the analysis is limited to near-nadir scans as discussed in section 3. Deeper PSs with afternoon (13–18 LT) echo-top heights well above 5 km over the Andes (e.g., 100 km mark) and in the morning (07–12 LT) over the foothills (e.g., 125 km mark) detected by GPM and missed by TRMM are a significant improvement that can be validated against rain gauge measurements (Barros, 2013; Eghdami & Barros, 2019). In contrast with TRMM, shallow precipitation with low echo-top heights (<5 km) is detected everywhere at all times of the day because of the KuPR's improved sensitivity and viewing geometry.

The clutter-free height is the lower altitude threshold for the detection of precipitation in complex terrain. An example (blue line) is shown in Figure 8 for one randomly selected GPM-DPR Ku-band NS swath overpass among all examined. Arulraj and Barros (2019) and Barros and Arulraj (2020) showed that contamination of near-surface reflectivity profiles due to ground clutter is the most important error source in GPM Ku-PR quantitative rainfall estimates in complex terrain. For instance, the contaminated region's height

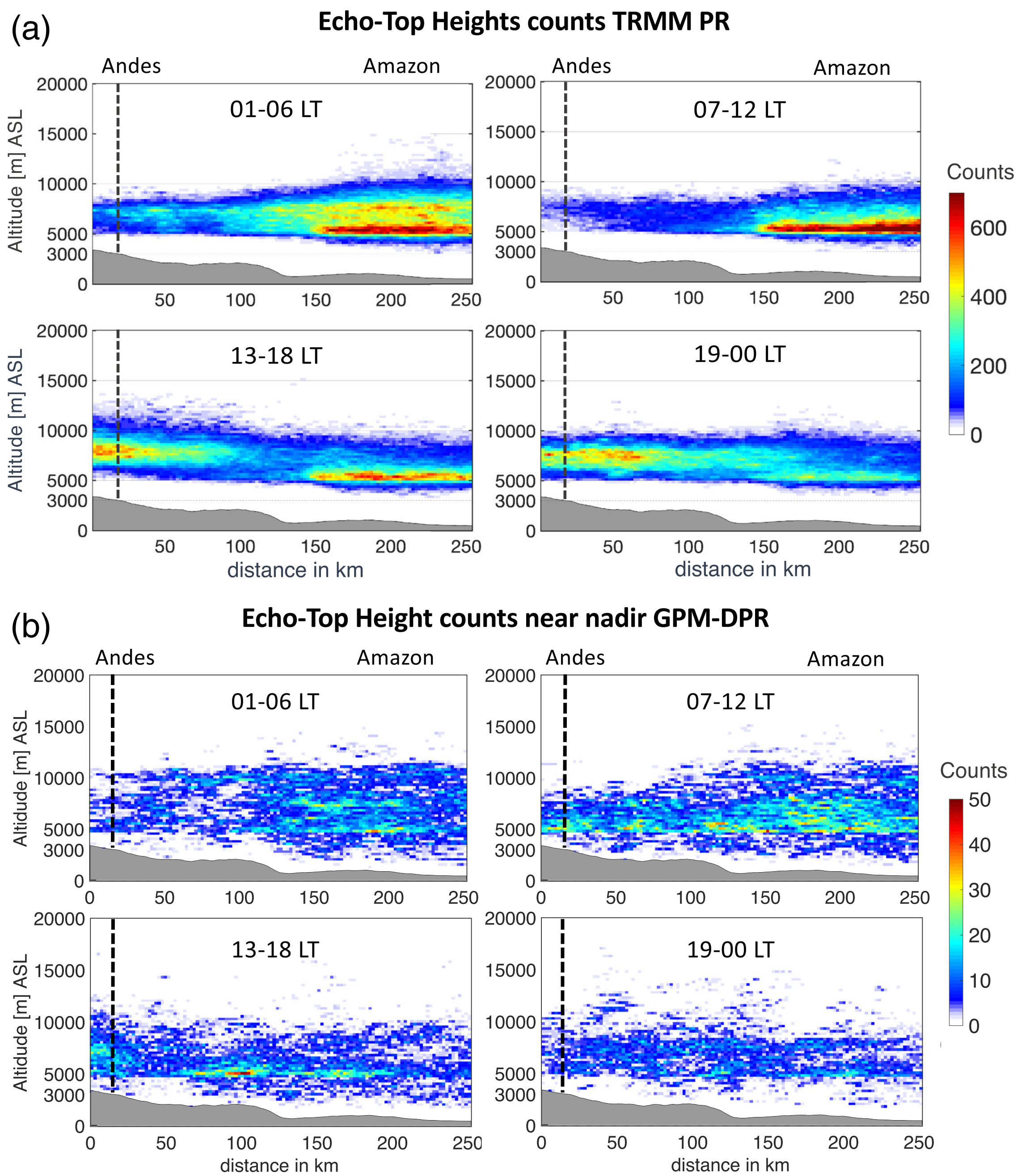

Figure 7. (a) Echo-top height counts in vertical bins of 200 m from the TRMM PR along west-east transects at 6-hr intervals. The gray area represents the mean terrain elevation. The transects range between 10°S and 13.5°S. The color scale is the total local count of echo-top heights. The vertical dashed line marks the Ka-band radar at LAMAR. (b) The same as (a) but from GPM DPR observations near the center of the swath (viewing angle <3.2°).

varies from 1.5–3 km AGL in the Southern Appalachian Mountains, depending on the radar view angle. In the MV, during the lifetime of the GPM DPR (2014–2019) examined here, the ground-clutter height ranges from 0.9–2.1 km AGL. Because of the high elevation (3,300 m ASL), the contaminated region's height is 44% of the time above the 0° isotherm, resulting in severe underestimation of rainfall. Furthermore, warm PSs, including LDPS with vertical development below the clutter-free height, are not detected.

4.1.2.2. Horizontal Structure: PFs

PFs obtained from the instantaneous TRMM and GPM swaths are aereal snapshots of PSs. Following CT17, TRMM PFs are categorized here according to aereal extent: small (25–2,250 km^2), medium

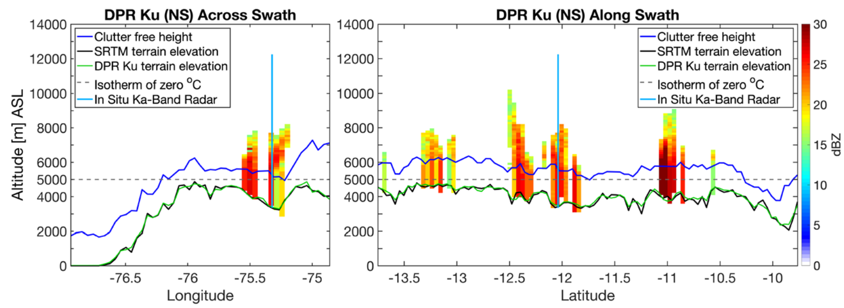

Figure 8. Example of GPM DPR Ku-band NS (Nadir Scan) cross sections of reflectivity across and along swath. Clutter-free height ~2 km. SRTM = Shuttle Radar Topography Mission.

(2,250–24,700 km^2) and large (>24,700 km^2). The large PFs that contribute most of the rainfall in the eastern slopes of the Andes (CT17) are not observed at MV's high elevation as expected due to dry conditions that inhibit the development of large convective systems (Mohr et al., 2014). Based on the TRMM swath retrievals (Iguchi, 2000), the contribution of small and medium PFs to MV rainfall is 75% and 25%, respectively (Figure 9). By disaggregating the contributions to the total rainfall into 6-hr intervals, it was found that afternoon (13–18 LT) small size PFs account for 41% of the TRMM daily rainfall based on 145 small-size PFs and 10 medium-size PFs in the record (Figure 9). Indeed, the number of small PFs is generally 1 order of magnitude higher than the number of medium-sized PFs at all times.

Summary statistics of the convective and stratiform contributions to total rainfall according to the TRMM PR 2A23 product classification (Awaka et al., 2009; Funk et al., 2013) are shown in black and white, respectively (Figure 9). On a daily scale, the principal contribution to the total TRMM rainfall in the MV comes from stratiform precipitation (60%). After disaggregating the rainfall in intervals of 6 hr (Figure 6), the contributions

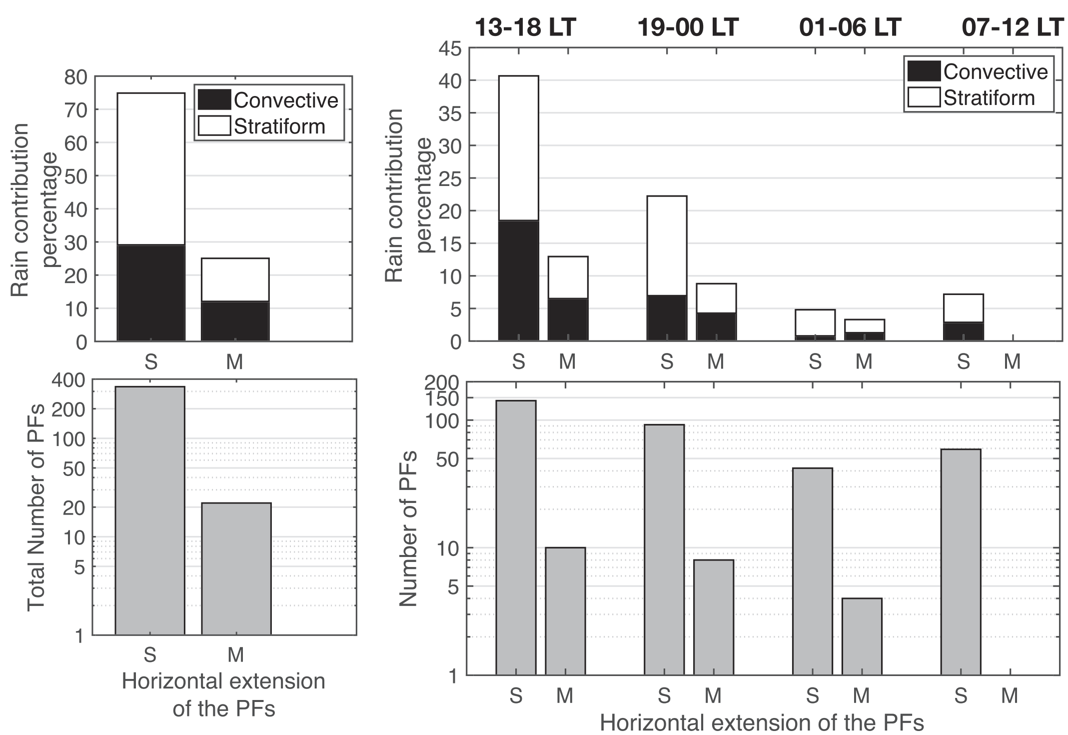

Figure 9. Climatology of small and medium-size PFs from TRMM PR 1998–2012 in the Mantaro Valley during the wet season (November–February). Top panels: overall contributions from convective (black) and stratiform (white) rainfall to the daily rain and as a function of time-of-day in percentage disaggregated in 6 hr intervals. Bottom panels: total number and frequency of small (S) and medium (M) size PFs as a function of time of day.

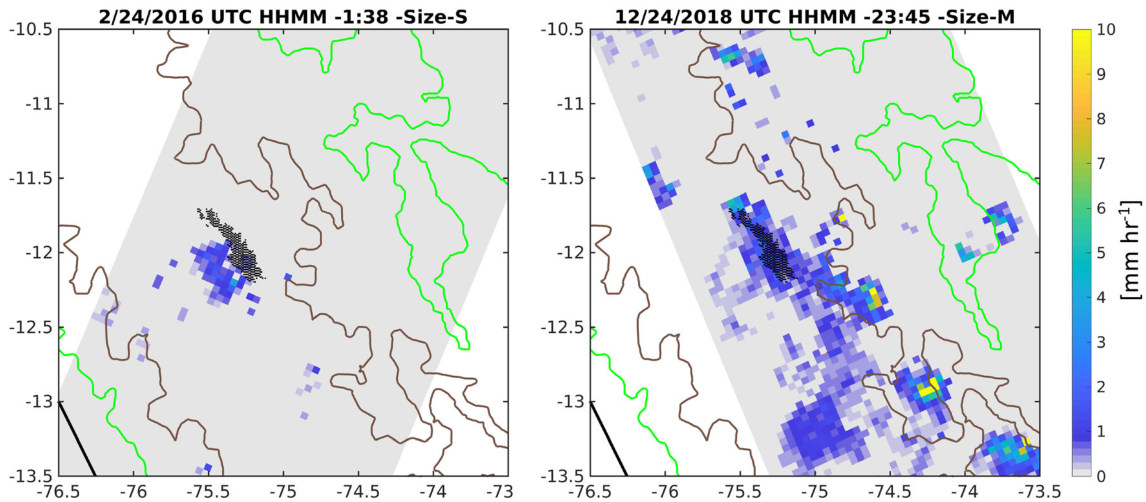

Figure 10. GPM DPR Ku-band radar swath retrievals show the spatial distribution of surface rainfall intensity [mm/hr, color scale] for a small (left panel) and a medium (right panel) size PFs over the Mantaro Valley (black dots). The 3,500 and 1,000 m ASL topographic contours are shown in brown and green, respectively. The title shows the date and hour of the acquisition of each swath.

of stratiform and convective precipitation remain around 60% and 40%, respectively, except during the early morning (01–06 LT) when the stratiform contribution is about 75%, and the convective contribution is 25%. Recall that this classification misses shallow PSs below the clutter-free height (Arulraj & Barros, 2017, 2019; Duan et al., 2015).

The spatial patterns of one small and one medium-size PFs obtained from GPM DPR Ku-band swaths are shown in Figure 10 for illustrative purposes. Based on the GPM DPR Ku-band swaths retrievals (Iguchi, 2018), the contribution of small and medium PFs is, respectively, 55% and 45% of MV rainfall (Figure 11). The 20% increase in the number of GPM DPR medium-size PFs is attributed to the DPR's higher sensitivity, viewing geometry, and algorithm changes (e.g., Liao & Meneghini, 2019) to improve detection of light rainfall that lead to larger PF aereal extent.

The principal contribution to the total GPM DPR rainfall in the MV comes from stratiform precipitation increasing from 60% to 70%. In contrast to the TRMM era, the rainfall contribution from medium PFs

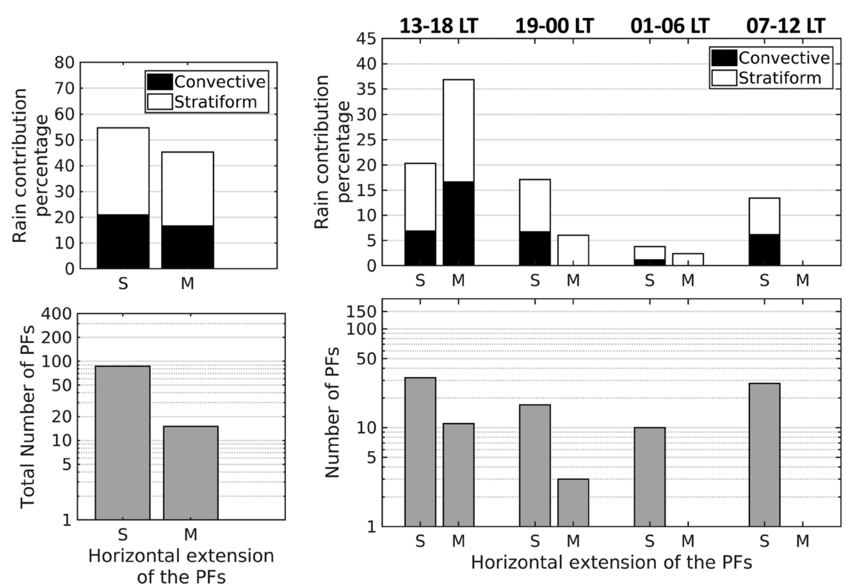

Figure 11. The same as Figure 6 but for GPM DPR Ku-band during 2014–2020.

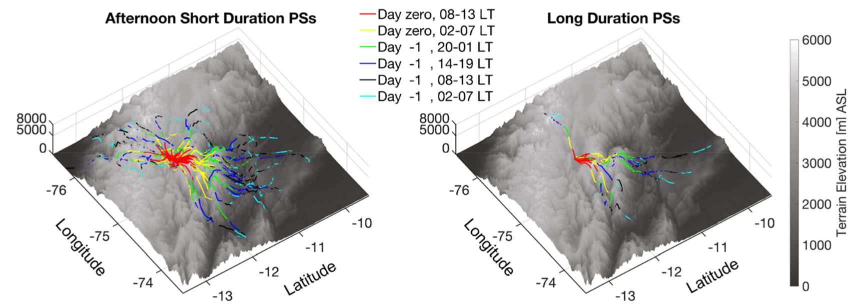

Figure 12. Temporal evolution of HYSPLIT trajectories that begin at 13 LT in the Mantaro Valley, for days when afternoon short (left) and long (right) duration precipitating systems were identified in January and February 2016–2018.

(37%) during the afternoon is higher than that of the small PFs (20%). There is an increase in the convective rainfall fraction in small PFs during the morning (07–12 LT) and in medium-size PFs during the afternoon (13–18 LT) consistent with the relative increases in echo-top heights reviewed earlier. During the remainder of the day, the rainfall contribution of small PFs is higher than medium size PFs in agreement with the TRMM-era.

A survey of GPM DPR PFs between 11 a.m. and 2 p.m. LT reveals infrequent small PFs (~1/month) producing light rainfall in the premonsoon season and higher rainfall rates in December and January when the convective fraction increases to ~50%. The frequency of small midday PFs doubles in February for mostly light stratiform rainfall. The high number of small raindrops at midday (Figure 4) is indicative of warm rain processes possibly including SFI among layered shallow clouds, which might be misclassified as an indication of convective activity depending on overpass geometry similar to what happens in the Southern Appalachians (Arulraj & Barros, 2019; Barros & Arulraj, 2020; Duan et al., 2015).

4.2. Interannual Variability of Precipitation

Among the 11 LDPSs detected at LAMAR, two events per season occur in 2016 and 2018, contributing 17% of January–February (JF) rainfall totals. In contrast, seven LDPSs produced 35% of JF rainfall in 2017. The significant year-to-year differences in frequency of LDPSs have significant implications in terms of precipitation totals and natural hazards. Persistent light rainfall saturates the landscape, leaving it more susceptible to flooding and landslides in response to heavy rain, such as in 2017. LDPSs play, therefore, a pivotal role in the high-elevation hydrometeorology of the central Andes. Next, the focus is on elucidating the interannual variability of LDPS from the regional moisture supply logistics perspective and on examining the specific synoptic staging that explains the interannual variability of the diurnal cycle of precipitation associated with LDPS.

4.2.1. Seasonal Moisture Sources

Previously, moisture advection from the eastern foothills of the Andes was associated with precipitation at higher elevations in the southern Andes of Peru in Cusco by Perry et al. (2017), and Endries et al. (2018) identified nocturnal long-duration stratiform PSs similar to the ones identified here at LAMAR. The moisture source regions for the afternoon short-duration PSs at LAMAR were linked to the eastern foothills and the Western Cordillera (Martínez-Castro et al., 2019; Moya-Álvarez et al., 2018). In the present study, wind backward trajectories for LDPSs and afternoon short duration PSs detected at LAMAR (following the methodology described in section 3.3) show that the principal moisture source is the low-level moisture convergence zone along the eastern Andes foothills (Figure 12; see also Sun & Barros, 2015a). For the 2016–2018 wet seasons, the trajectories originating from the western Cordillera and the Andes' eastern slopes account for 10% and 75% of the total seasonal rainfall, respectively. Afternoon short-duration PSs and nocturnal LDPSs explain 85% of MV seasonal rainfall, the remainder 15% corresponding to short duration PSs at different times of the day. Moist air reaching LAMAR at 13 LT comes from adjacent ridges (02–13 LT), which in turn can be traced back to lower elevation upwind valleys and ridges down to the foothills over 2 days (Figure 12). The dependability of definite moisture source regions along the eastern Andes foothills is therefore key to dependable precipitation at high elevations.

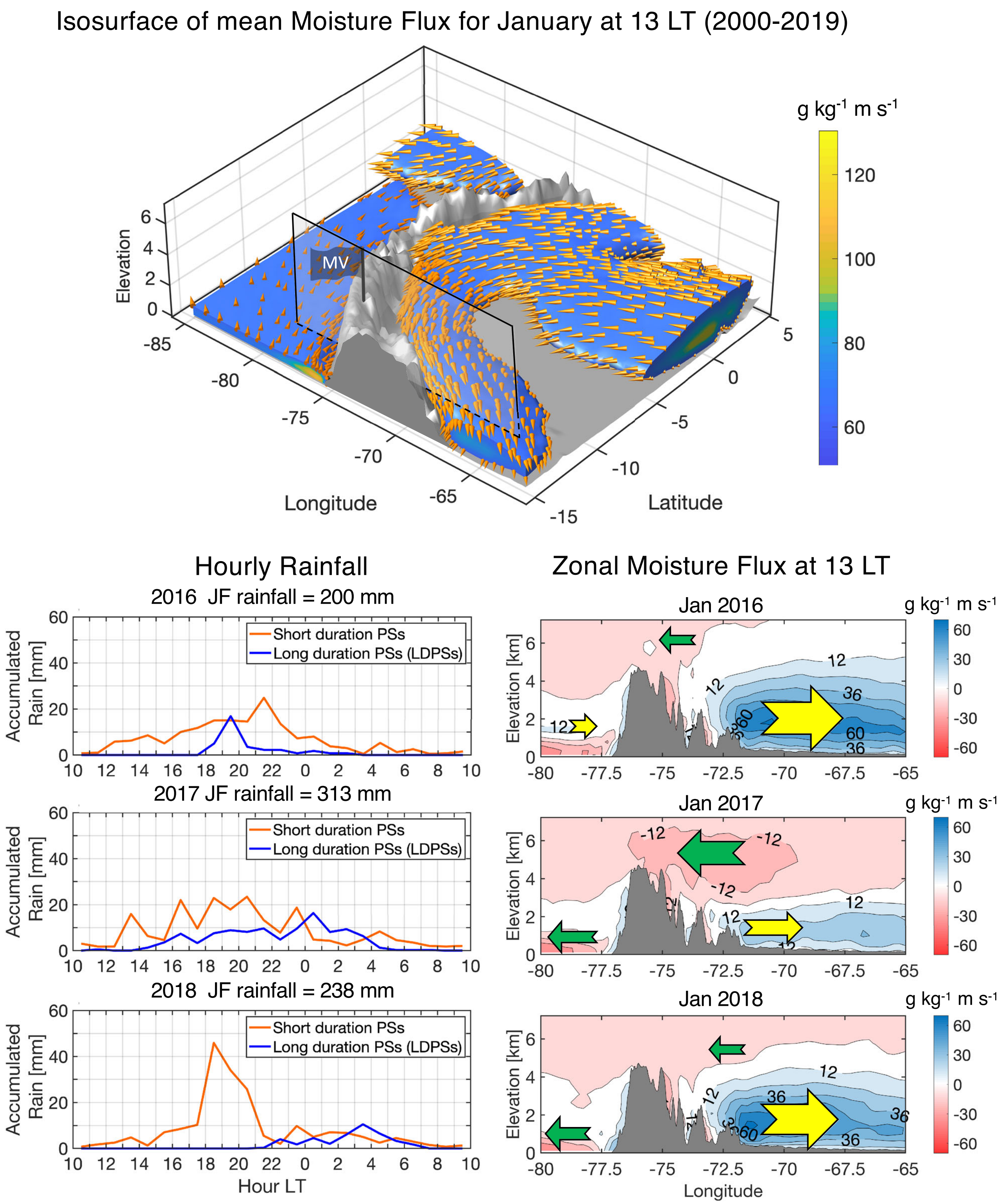

Figure 13. Top: climatological (2000–2019) January SALLJ MF delimited by an isosurface of mean moisture flux (MF; 60 g kg^{-1} ms^{-1}) at 13 LT obtained from ERA5 reanalysis. The orientation of the orange cones depicts wind direction. The Andes topography is the gray surface. The vertical box marks the cross section. The black flag indicates the location of the MV. Bottom left column: accumulated rainfall during January and February for years 2016–2018 at different hours. Blue = LDPS; orange = short duration (<6 hr) PSs. Bottom right column: cross sections at 12°S of January mean zonal MF 2016–2018 at 13 LT. Blue shades and yellow arrows = eastward zonal MF. Red shades and green arrows = westward zonal MF. The size of the arrows is indicative of MF magnitude.

Table 2
Summary of Most Common ENSO Indexes Corresponding to SST Anomalies at Different Locations and Time Scales

Year	Month	E	C	Region 1.2	Region 3	ONI JFM	JF rain (mm) LAMAR
2016	1	1.87	1.93	1.81	2.59	2.2	200
2016	2	1.18	1.95	1.38	1.97		
2017	1	0.44	−0.79	0.95	−0.08	−0.1	313
2017	2	0.79	−0.70	1.44	0.42		
2018	1	−1.04	−1.18	−1.10	−1.19	−0.8	238
2018	2	−0.91	−0.98	−0.89	−0.91		

Note. ONI is the Oceanic Niño Index. The last column shows the accumulated January–February (JF) rainfall measured at LAMAR in the Mantaro Valley.

In turn, the dependability of moisture source regions is tied to large-scale mechanisms of moisture convergence along the eastern Andes, specifically the SALLJ and CAIs. The SALLJ can occur simultaneously or separately in the northern and central Andes (e.g., Jones, 2019). The January climatology (2000–2019) of the mean structure of the SALLJ at 13 LT shows that the SALLJ is in close alignment with the topography east of MV (Figure 13). Consequently, moisture transport with NW-SE orientation at 12°S has a large eastward component (i.e., away from the terrain). Further south, at the Fitzcarrald Arch (13–13.5°S; Regard et al., 2009), the SALLJ turns and acquires a significant westward component that brings moisture toward the eastern slopes of the Andes (Figure 13; CT17; Espinoza et al., 2015). Moisture transport to the central Andes is linked, therefore, to SALLJ morphology and orientation at 12°S.

Figure 13 also shows the zonal MF at 13 LT in January of 2016–2018 along a cross section at 12°S. The zonal MF is positive (to the east) at low elevations (~2,000 m) east of MV and negative (to the west) at midlevels (altitudes above 4,000 m) in 2017 when the low-level MF into the foothills strengthens. A similar analysis for February is available in the supporting information (Figure S3). This suggests that one or both characteristics of the zonal MF, that is, the increase in westward MF at middle and low levels, explain the ~35% increase in JF cumulative rainfall in 2017 relative to 2016 and 2018.

Table 2 summarizes ENSO activity 2016–2018. In JFM of 2016, a very strong El Niño was identified in Region 3.4 (L'Heureux et al., 2017; Rasmusson & Carpenter, 1982), and the Oceanic Niño Index (ONI) was 2.2. In 2017, the ONI index was neutral. However, the SST anomalies in Region 1.2 are very high, consistent with El Niño Costero conditions (Takahashi & Martínez, 2019). In JFM of 2018, the ONI index and the SST anomalies in Regions 1.2 and 3.4 indicate moderate La Niña conditions. Earlier studies (Ferreira et al., 2003; Marengo et al., 2004) demonstrated that the SALLJ was stronger and more frequent during DJF of the 1998 El Niño than in the same months of the 1999 La Niña. This result was generalized in a recent climatology by Montini et al. (2019), who report that SALLJ days are more frequent during DJF of El Niño years than during DJF of neutral years. Thus, the mean zonal MF during January 2016 (El Niño year) represents a month with a high SALLJ frequency. Inspection of the climatology of CAIs (1979–2017) conducted by Eghdami and Barros (2019) reveals seven CAIs during January and February of 2017 and only two in January and February of 2016 (Table 3).

Table 3
Date When LDPS Were Detected in the Mantaro Valley (12°S) and the Date When the Nearest Cold Air Incursion (CAI) Was Identified (Eghdami & Barros, 2019)

LDPS	LDPS day	Synoptic regime	CAI day
1	2/11/2016	SALLJ	2/9/2016
2	2/28/2016	SALLJ	—
3	1/4/2017	SALLJ	1/5/2017
4	1/15/2017	SALLJ	1/11/2017
5	1/19/2017	CAI	1/18/2017
6	1/24/2017	CAI Transition	1/18/2017 and 1/26/2017
7	1/26/2017	CAI	1/26/2017
8	2/16/2017	CAI Transition	2/14/2017 and 2/19/2017
9	2/22/2017	CAI	2/19/2017
10	1/16/2018	SALLJ	—
11	1/17/2018	SALLJ	—

Note. Day 0 is the day when a CAI is formally detected as it reaches the tropics (55.5–60°W and 22.50–27.00°S). The synoptic regime classes are defined based on the inspection of moisture flux maps at 850 and 750 hPa (see Figures 14–16).

Next, the zonal MF in 2016 and 2017 was examined on a month-by-month basis for each year and each LDPS separately. In January of 2016, the eastward zonal MF was the strongest in the 3 years analyzed here; thus, less moisture reaches the Andes, and no LDPS occurred in the MV. In February of the same year, the eastward moisture transport weakened, and two LDPS were detected in the MV. The back trajectories for these 2 days originate in the eastern foothills, and the total amount of rainfall measured in January and February of 2016 was 200 mm. In January of 2017, the low-level moist convergence is considerable (and conversely, the eastward zonal MF was the weakest). At midlevels (2–6 km), the MF

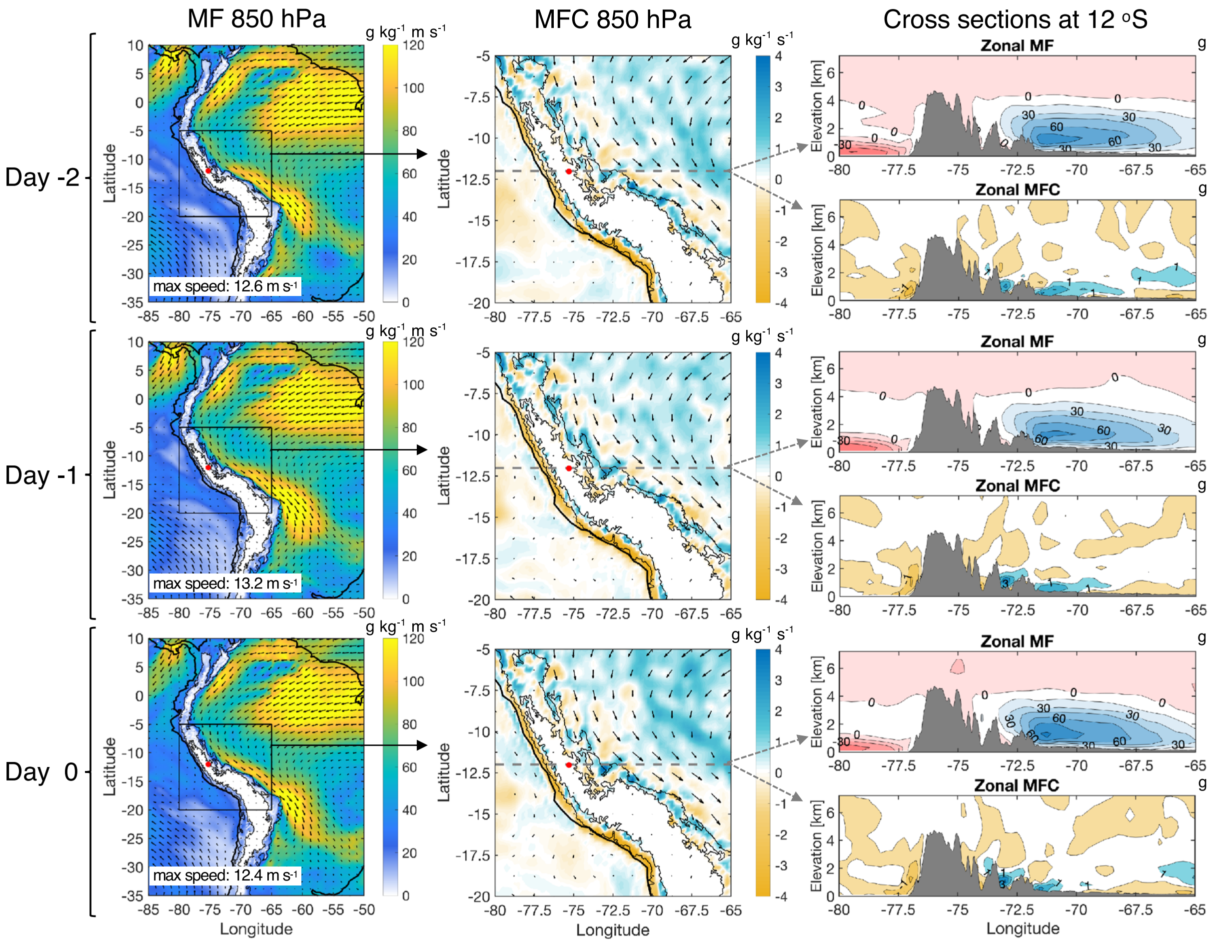

Figure 14. SALLJ conditions. Analysis of moisture flux (MF) and moisture flux convergence (MFC) for each day relative to the occurrence of LDPS at MV (day 0). Left: mean daily MF and winds at 850 hPa. Center: mean daily MFC and winds at 850 hPa. Right: cross sections at 12°S of mean daily zonal MF (top) and MFC (bottom). The red dot marks the MV. The gray dashed line marks the 12°S cross section. The thin black lines are the 1,000 and 3,500 m elevation contour lines. MFC values are multiplied by 10^4.

toward the Andes was the largest in the 3 years studied here. The northward propagation of the CAI front decreases the low-level eastward MF and increases the westward MF at midlevels. Under these favorable conditions, five LDPS were identified in the MV, with the back trajectories of four traced to the eastern foothills and only one originating from the western Andes Cordillera. During February of 2017, two CAIs occurred. Despite a decrease at low levels, the midlevel MF is similar to January of 2017. In January of 2018, the eastward low-level MF was more substantial than in January of 2017 but weaker than in January of 2016, and two LDPS were located in the MV with trajectories linked to the eastern foothills. No LDPSs were found in the MV in February of 2018. MV JF rainfall in 2017 was 313 mm, 35% of which was associated with LDPSs that explain ~2/3 of the rainfall accumulation difference between 2016 and 2017. The total accumulation in January and February of 2018 was 238 mm, close to 2016 values.

The data suggest that the interannual variability of monsoon precipitation is explained by changes in the frequency of LDPS in the High Andes and that synoptic-scale circulations govern LDPS frequency in the Western Amazon by organizing moisture source regions along the eastern Andes foothills and easterly MF at midlevels. Large MF at midlevels is the distinguishing factor that controls the intraseasonal frequency of LDPS. The role of large-scale conditions such as ENSO teleconnections is challenging to ascertain, given the short duration of the ground validation data available at LAMAR.

4.2.2. Synoptic Precursors of LDPS

Analysis of MV LDPS on a case-by-case basis point to three distinct classes of synoptic-scale precursors according to regional meteorology (Table 2): (1) SALLJ; (2) northward propagation phase Cold Air

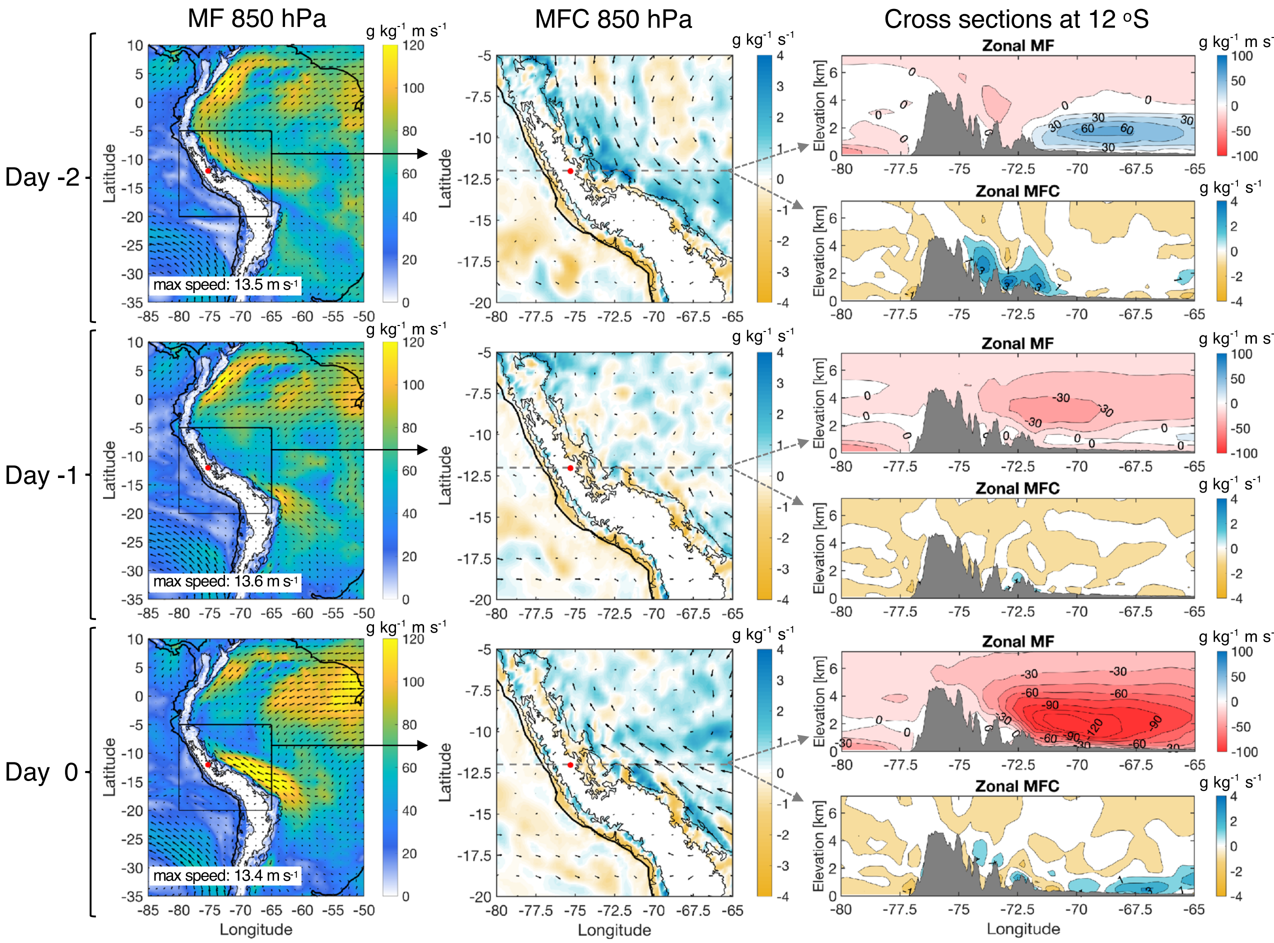

Figure 15. The same as Figure 14 but for CAI conditions.

Incursions (CAI); and (3) CAI transition (CAI-T) when the LDPS occurs late in the CAI retreat phase and before the next one reaches the tropics. In 2016 and 2018, the LDPS (two in each year) occurred on days associated with SALLJ conditions. In 2017, two LDPS were tied to the SALLJ, three to CAI, and two to CAI-T. For each category, the mean daily zonal MF, the 850 hPa MFC maps, and cross sections at 12°S for the LPDS day (Day 0) and the two previous days (Days −1 and −2) are presented in Figures 14–16. Because 10 of 11 LDPS are nocturnal, the mean daily flux values corresponding to Day 0 (zero) are calculated for the 24 hr starting at 19 LT.

Under SALLJ conditions, a narrow and shallow band of high values of MFC (2×10^{-4}–3×10^{-4} g kg^{-1} s^{-1}) forms along the 1,000 m topographic contour (Figure 14). It reaches up to 1,500 m and is characterized by the highest MFC values in the Andes' most eastern foothills near the surface. By contrast, CAIs produce high MFC along a broader region around the 1,000 m contour (Figures 15 and 16), with high MFC penetrating the inner Andes and reaching altitudes up to 3 km. The differences in MF between Days −2 and 0 for the SALLJ category are small. The CAI forward propagation into the western Amazon basin along the Andes and subsequent retreat significantly reorganize regional moisture convergence patterns over the Andes (CAI and CAI-T synoptic regimes). The zonal MF in Figure 14 shows a SALLJ structure (similar to January of 2016; Figure 13) during Days −2, −1, and 0, with a slight increase in Day 0 MF. The foothills are, therefore, the source of moisture to the MV 1–2 days before the LDPS.

Figure 15 shows MF and winds for CAI conditions during Day 0 along the foothills of the Andes between 10° and 20°S following weak SALLJ conditions in Day −2. On Day −1, the northern SALLJ is cut off, and winds are very weak in the central Andes between 5° and 12°S. At the same time, the approach of the CAI front is

10.1029/2020JD032947

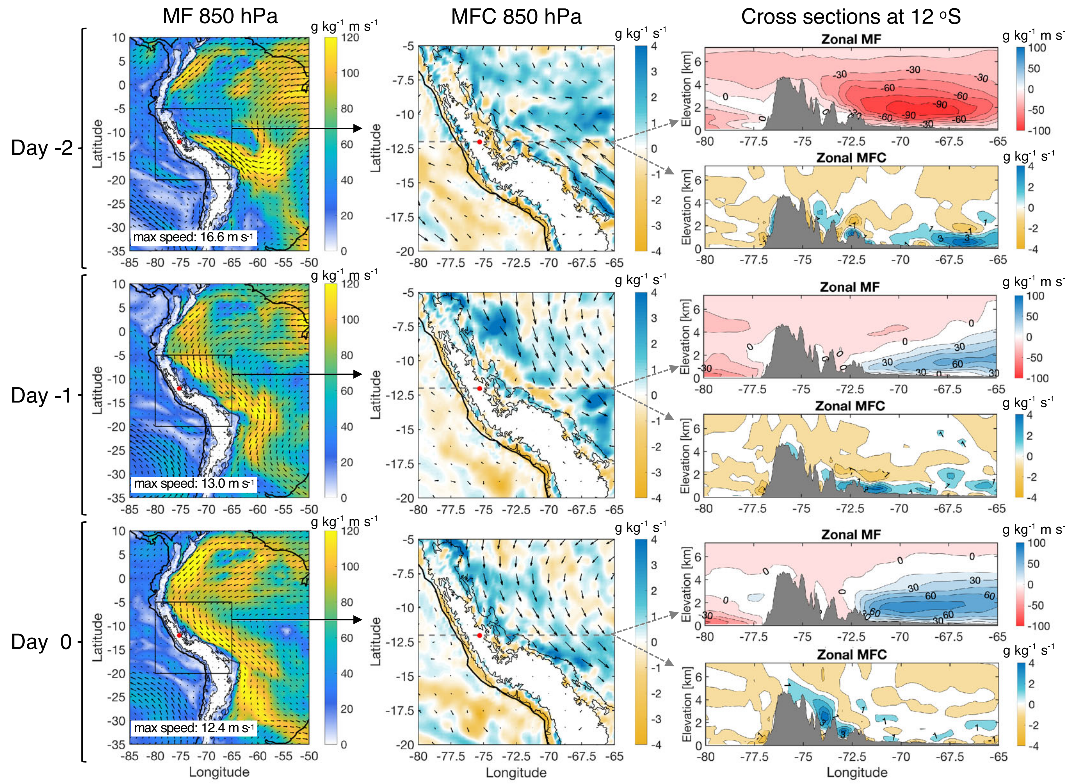

Figure 16. The same as Figure 14 but for CAI-T conditions.

already apparent with strong southeasterly winds south of 12°S. The front latches to the central Andes' eastern slopes as it propagates further northwestward in Day 0. The MFC map at 850 hPa (Figure 15) from Days −2 to 0 shows values ranging between 2×10^{-4} and 4×10^{-4} g kg^{-1} s^{-1} in the foothills of the Andes around 12°S. Weak MF at low levels in Day −2 is followed by strong low-level and midlevel westward MF on Day 0, the CAI arrival. On Day −2, the MFC is high (~3×10^{-4} g kg^{-1} s^{-1}) below 2,000 m above the foothills and extends from the surface up to 3,000 m at 74°W toward the inner region. The additional moisture availability at 3,000 m before the CAI arrival suggests that moisture needs to travel shorter distances to reach higher heights in the Central Andes and explains the association of snowfall at the Quelcaya glacier in Cusco to CAI events (Hurley et al., 2015).

Figure 16 illustrates CAI-T conditions along the foothills of the Andes between 10°S and 20°S. Note how the conditions in Day −2 are very similar for the CAI case in Day 0 with the difference that the CAI is beginning to retreat. In Day −1, the central SALLJ connects to the northern SALLJ. Still, the core remains away from the foothills. It only recovers fully by Day 0 with strong moisture convergence along the foothills and the eastern slopes up to 5 km elevation, reaching the high-elevation inner valleys in the central Andes. The 850 hPa mean daily zonal MFC map on Day −2 is similar to Day 0 in the CAI category (Figure 15) with values in the range between 2×10^{-4} and 4×10^{-4} g kg^{-1} s^{-1}. Likewise, the zonal MF cross section on Day −2 has CAI structure. The zonal MF resembles a weak SALLJ in Day −1. The SALLJ structure apparent in Day 0 is similar to Day −2 in the CAI category (Figure 15).

In summary, high MFC in the eastern foothills of the central Andes around 12°S occurs 1–2 days ahead of a CAI arrival. It persists for 1–2 days as the CAI recedes and the SALLJ strengthens, respectively, for CAI and CAI-T LDPS. The large MFC (~3×10^{-4} g kg^{-1} s^{-1}) extends from the surface up to ~2,000 m along the easternmost ridges (73–72°W) and penetrates to ~3,000 m and higher to the west (74°W) as the CAI front serves as a dynamic guide to midlevel MFC. For SALLJ conditions, the low-level MFC is shallower (~below 1,500 m) and confined to the eastern foothills during the 2 days before the LDPS in agreement with the 2 day time scale for upslope moisture transport from the foothills to the MV as shown in section 4.2.1.

5. Conclusion

Observations from the GPM dual-polarization radar (DPR), TRMM PR, ground-based radars, rain gauges, and an optical disdrometer were used to characterize the diurnal cycle of precipitation and interannual variability of monsoon precipitation at high elevations in the central Andes of Peru.

5.1. Diurnal Cycle

Convective activity is dominant in the afternoon and early evening (15–20 LT) when the highest rainfall intensity and larger drop sizes are observed at LAMAR. Stratiform precipitation with bright-band prevails during the night and early morning (20–06 LT). Storm echo-top heights are higher (up to 13 km ASL) between 13 and 18 LT in the High Andes than in the foothills, and the reverse is true at night. The increase in the frequency and altitude of daytime eco-top heights-based GPM DPR Ku-band reflectivity profiles relative to the TRMM PR climatology is attributed mainly to improvements in radar sensitivity.

A 20-year climatology of the spatial structure of the PSs that affect the MV was developed based on the analysis of 15 years of TRMM PR (1998–2012) and 6 years of GPM DPR (2014–2020) observations. The results show that the MV climatology is dominated by small and medium-size PFs in contrast with large PFs in the Andes foothills (CT17). Small-size PFs in the afternoon (12–18 LT) produce 40% and 20% of the daily rainfall, according to TRMM PR and GPM DPR, respectively. The ratio between convective and stratiform rain is 45/55 and 38/62. During the night (19–00 LT), the proportion of stratiform over convective precipitation is higher, with stratiform precipitation amounting to 58% and 65% of total rainfall estimated from TRMM PR and GPM DPR measurements, respectively, in agreement with previous global studies (e.g., Funk et al., 2013). Nevertheless, bias due to ground-clutter contamination of satellite-based radar measurements over complex terrain must not be overlooked. Retrieval algorithms cannot detect precipitation below the clutter-free height (i.e., the blind zone). There are a high number of missed detections, while rain-rate estimates are significantly lower than ground-based observations (Barros & Arulraj, 2020; Duan et al., 2015). Furthermore, retrieval algorithms that rely on the presence of a bright band to classify precipitation as stratiform fail if the 0° isotherm is below the clutter-free height (Awaka et al., 2009). Indeed, the MV topography is a significant challenge for GPM DPR with the clutter-free height ranging between 900 and 2,100 m ASL and above the 0° isotherm (~5,000 m ASL) 44% of the time.

LDPSs evolve from afternoon embedded convection (predominantly in the late afternoon, albeit early also as in 2017) in the valley into nighttime stratiform rainfall. They often persist until the early morning of the next day and make a distinctive contribution to monsoon precipitation at high elevations. LDPS events contribute approximately 25% of the wet season rainfall in MV for the 2016–2018 period of study. Previously, Perry et al. (2017) and Endries et al. (2018) identified similar LDPS to the south into Bolivia. LDPSs emerge, therefore, as the principal mode of nighttime precipitation at high elevations in the Central Andes.

5.2. Interannual Variability

Hot spots of moisture convergence along the Central Andes' eastern foothills are the moist source for LDPSs in the MV. Interannual changes in the spatial organization of moisture source regions impact the diurnal cycle of precipitation at high elevations. In particular, LDPS moisture source regions are determined by the interaction of the SALLJ with the eastern Andes foothills and by CAI activity, with broader and deeper moisture pooling against the foothills associated with the latter. For SALLJ conditions, moisture convergence occurs 1–2 days prior and on the same day of detecting an LDPS in the most eastern slopes facing the Amazon. Moisture convergence is enhanced along the CAI front at low levels against the eastern foothills (74°W) and midlevels 1–2 days before detecting an LDPS. This 1–2 day time scale is in keeping with the transport time scale from the Central Peruvian Andes' eastern foothills to the MV inferred from the back trajectory analysis.

Analysis of synoptic-scale conditions using ERA5 indicates that enhanced easterly MFC at midlevels (2–6 km) is necessary to explain increases in LDPSs frequency. For instance, when the number of CAIs increased from 1 to 6 in JF of 2017, the number of LDPSs increased from 2 two 7, leading to a 56.5% increase in total rainfall accumulation relative to 2016. The CAI fronts work as a guide to organize the midlevel moisture ahead of the front in the northward propagation phase and, or behind it in the retreat phase (e.g., Eghdami & Barros, 2019).

5.3. Summary

This study articulates a novel hypothesis that explains monsoon precipitation's interannual variability at high elevations in the Central Andes in terms of LDPS frequency and CAI activity. Nevertheless, a note of caution is warranted due to the short record-length of ground-based observations available (3 years) and the relatively small number of LDPSs identified (11 events). The lack of long records and strategically placed mesoscale observing systems poses a significant research challenge in the region. Ongoing work seeks to develop a climatology of LDPS by proxy based on large-scale circulation patterns favorable to moisture convergence at midlevels from ERA5. However, reanalysis does not capture the nonlinear interactions among weather dynamics, topography, and land cover that govern orographic precipitation processes in the eastern slopes of the Central Andes (e.g., Eghdami & Barros, 2019, 2020). Therefore, high-resolution modeling studies are necessary in the future to elucidate the mesoscale dynamics of LDPS at high elevations.

Data Availability Statement

The TRMM and GPM data used in this effort were acquired as part of the activities of NASA's Science Mission Directorate and are archived and distributed by the Goddard Earth Sciences (GES) Data and Information Services Center (DISC). The ground-based data used in this study, that is, Ka-band radar, wind radar, disdrometer, and rain gauge data, are available from Duke University repositories (https://doi.org/10.7924/r41n84j94).

Acknowledgments

The authors gratefully acknowledge the NOAA Air Resources Laboratory (ARL) for the provision of the HYSPLIT transport and dispersion model and READY website (http://www.ready.noaa.gov) used in this publication. We thank Dr. Danny Scipion for help processing the wind radar data and the team that maintains the instruments at the Huancayo observatory and LAMAR laboratory from the Instituto Geofísico del Perú (IGP). The authors acknowledge the Copernicus Climate Change Service (C3S) (2017): ERA5: Fifth generation of ECMWF atmospheric reanalyses of the global climate, Copernicus Climate Change Service Climate Data Store (CDS), 2019. (http://cds.climate.copernicus.eu/cdsapp#!/home). The first author acknowledges support from Fondecyt Peru for his doctoral fellowship (Contract No. 2017-14). Innovate Peru supported the second author (Contract No. 400-PNICP-PIBA-2014). This work was supported in part by NASA Grant 80NSSC19K0685 with the corresponding author.

References

Angulo-Martínez, M., & Barros, A. P. (2015). Measurement uncertainty in rainfall kinetic energy and intensity relationships for soil erosion studies: An evaluation using PARSIVEL disdrometers in the Southern Appalachian Mountains. *Geomorphology*, *228*, 28–40.

Arulraj, M., & Barros, A. P. (2017). Shallow precipitation detection and classification using multifrequency radar observations and model simulations. *Journal of Atmospheric and Oceanic Technology*, *34*(9), 1963–1983. https://doi.org/10.1175/jtech-d-17-0060.1

Arulraj, M., & Barros, A. P. (2019). Improving quantitative precipitation estimates in mountainous regions by modelling low-level seeder-feeder interactions constrained by Global Precipitation Measurement Dual-frequency Precipitation Radar measurements. *Remote Sensing of Environment*, *231*, 111213. https://doi.org/10.1016/j.rse.2019.111213

Awaka, J., Iguchi, T., & Okamoto, K. I. (2009). TRMM PR standard algorithm 2A23 and its performance on bright band detection. *Journal of the Meteorological Society of Japan. Ser. II*, *87*, 31–52. https://doi.org/10.2151/jmsj.87A.31

Barros, A. P. (2013). Orographic precipitation, freshwater resources, and climate vulnerabilities in mountainous regions. In J. Adegoke, & C. Y. Wright (Eds.), *Climate Vulnerability: Understanding and Addressing Threats to Essential Resources* (Vol. 1, pp. 57–78). Waltham, MA: Elsevier Inc.; Academic Press. https://doi.org/10.1016/B978-0-12-384703-4.00504-9

Barros, A. P., & Arulraj, M. (2020). Remote sensing of orographic precipitation. In *Satellite Precipitation Measurement* (pp. 559–582). Cham: Springer.

Barros, A. P., Kim, G., Williams, E., & Nesbitt, S. W. (2004). Probing orographic controls in the Himalayas during the monsoon using satellite imagery. *Natural Hazards and Earth System Science*, *4*(1), 29–51. https://doi.org/10.5194/nhess-4-29-2004

Barros, A. P., & Lettenmaier, D. P. (1994). Dynamic modeling of orographically induced precipitation. *Reviews of Geophysics*, *32*(3), 265–284.

Biasutti, M., Yuter, S. E., Burleyson, C. D., & Sobel, A. H. (2012). Very high-resolution rainfall patterns measured by TRMM precipitation radar: Seasonal and diurnal cycles. *Climate Dynamics*, *39*(1–2), 239–258. https://doi.org/10.1007/s00382-011-1146-6

Campetella, C. M., & Vera, C. S. (2002). The influence of the Andes mountains on the South American low-level flow. *Geophysical Research Letters*, *29*(17), 7–1. https://doi.org/10.1029/2002GL015451

Chavez, S. P., & Takahashi, K. (2017). Orographic rainfall hot spots in the Andes-Amazon transition according to the TRMM precipitation radar and in situ data. *Journal of Geophysical Research: Atmospheres*, *122*, 5870–5882. https://doi.org/10.1002/2016JD026282

Chevallier, P., Pouyaud, B., Suarez, W., & Condom, T. (2011). Climate change threats to the environment in the tropical Andes: Glaciers and water resources. *Regional Environmental Change*, *11*(1), 179–187. https://doi.org/10.1007/s10113-010-0177-6

Dee, D. P., Uppala, S. M., Simmons, A. J., Berrisford, P., Poli, P., Kobayashi, S., et al. (2011). The ERA-Interim Reanalysis: Configuration and performance of the data assimilation system. *Quarterly Journal of the Royal Meteorological Society*, *137*(656), 553–597. https://doi.org/10.1002/qj.828

Duan, Y., & Barros, A. P. (2017). Understanding how low-level clouds and fog modify the diurnal cycle of orographic precipitation using in situ and satellite observations. *Remote Sensing*, *9*(9), 920.

Duan, Y., Wilson, A. M., & Barros, A. P. (2015). Scoping a field experiment: Error diagnostics of TRMM precipitation radar estimates in complex terrain as a basis for IPHEx2014. *Hydrology and Earth System Sciences*, *19*(3), 1501–1520. https://doi.org/10.5194/hess-19-1501-201

Eghdami, M., & Barros, A. P. (2019). Extreme orographic rainfall tied to cold air intrusions in the eastern Andes. *Frontiers in Earth Sciences - Atmospheric Science*, *7*, 101. https://doi.org/10.3389/fenvs.2019.00101

Eghdami, M., & Barros, A. P. (2020). Deforestation impacts on orographic precipitation in the tropical Andes. *Frontiers Environmental Sciences – Atmospheric Science* in press. https://doi.org/10.1002/essoar.10503773.1

Endries, J. L., Perry, L. B., Yuter, S. E., Seimon, A., Andrade-Flores, M., & others, m. (2018). Radar-observed characteristics of precipitation in the tropical high Andes of southern Peru and Bolivia. *Journal of Applied Meteorology and Climatology*, *57*(7), 1441–1458. https://doi.org/10.1175/JAMC-D-17-0248.1

Espinoza, J. C., Chavez, S., Ronchail, J., Junquas, C., Takahashi, K., & Lavado, W. (2015). Rainfall hotspots over the southern tropical Andes: Spatial distribution, rainfall intensity, and relations with large-scale atmospheric circulation. *Water Resources Research*, *51*, 3459–3475. https://doi.org/10.1002/2014WR016273

Espinoza, J. C., Ronchail, J., Lengaigne, M., Quispe, N., Silva, Y., Bettolli, M. L., et al. (2013). Revisiting wintertime cold air intrusions at the east of the Andes: Propagating features from subtropical Argentina to Peruvian Amazon and relationship with large-scale circulation patterns. *Climate Dynamics*, *41*(7–8), 1983–2002. https://doi.org/10.1007/s00382-012-1639-y

Ferreira, R. N., Rickenbach, T. M., Herdies, D. L., & Carvalho, L. M. (2003). Variability of South American convective cloud systems and tropospheric circulation during January–March 1998 and 1999. *Monthly Weather Review*, *131*(5), 961–973.

Flores, J. L., Alvarez, A. S., Kumar, S., Martínez, D., Villalobos, E., & Silva, Y. (2019). Analysis of Possible Triggering Mechanisms of Severe Thunderstorms in the Tropical Central Andes of Peru, Mantaro Valley. *Atmosphere*, *10*(6), 301. https://doi.org/10.3390/atmos10060301

Francou, B., Vuille, M., Favier, V., & Cáceres, B. (2004). New evidence for an ENSO impact on low-latitude glaciers: Antizana 15, Andes of Ecuador, 0 28′S. *Journal of Geophysical Research: Atmospheres*, *109*, D18106. https://doi.org/10.1029/2003JD004484

Funk, A., Schumacher, C., & Awaka, J. (2013). Analysis of rain classifications over the tropics by Version 7 of the TRMM PR 2A23 algorithm. *Journal of the Meteorological Society of Japan. Ser. II*, *91*(3), 257–272. https://doi.org/10.2151/jmsj.2013-302

Giovannettone, J. P., & Barros, A. P. (2009). Probing regional orographic controls of precipitation and cloudiness in the central Andes using satellite data. *Journal of Hydrometeorology*, *10*(1), 167–182. https://doi.org/10.1175/2008JHM973.1

Hamada, A., & Takayabu, Y. N. (2016). Improvements in detection of light precipitation with the global precipitation measurement dual-frequency precipitation radar (GPM DPR). *Journal of Atmospheric and Oceanic Technology*, *33*(4), 653–667. https://doi.org/10.1175/JTECH-D-15-0097.1

Hersbach, H., Bell, B., Berrisford, P., Hirahara, S., Horányi, A., Muñoz-Sabater, J., et al. (2020). The ERA5 global reanalysis. *Quarterly Journal of the Royal Meteorological Society*, *146*, 1999–2149. https://doi.org/10.1002/qj.3803

Houze, R. A. Jr. (2014). *Cloud dynamics*. Academic Press.

Huffman, G. J., Bolvin, D. T., Braithwaite, D., Hsu, K., Joyce, R., Xie, P., & Yoo, S. H. (2015). NASA global precipitation measurement (GPM) integrated multi-satellite retrievals for GPM (IMERG). Algorithm Theoretical Basis Document (ATBD) Version, 4, 26.

Hurley, J. V., Vuille, M., Hardy, D. R., Burns, S. J., & Thompson, L. G. (2015). Cold air incursions, δ^{18}O variability, and monsoon dynamics associated with snow days at Quelccaya Ice Cap, Peru. *Journal of Geophysical Research: Atmospheres*, *120*, 7467–7487. https://doi.org/10.1002/2015JD023323

Iguchi, T., Kozu, T., Meneghini, R., Awaka, J., & Okamoto, K. I. (2000). Rain-profiling algorithm for the TRMM precipitation radar. *Journal of Applied Meteorology*, *39*(12), 2038–2052.

Iguchi, T., Meneghini, R., Awaka, J., Kozu, T., & Okamoto, K. (2000). Rain profiling algorithm for TRMM precipitation radar data. *Advances in Space Research*, *25*(5), 973–976. https://doi.org/10.1016/S0273-1177(99)00933-3

Iguchi, T., Kozu, T., Kwiatkowski, J., Meneghini, R., Awaka, J., & Okamoto, K. I. (2009). Uncertainties in the rain profiling algorithm for the TRMM precipitation radar. *Journal of the Meteorological Society of Japan. Ser. II*, *87*, 1–30.

Iguchi, T., Seto, S., Meneghini, R., Yoshida, N., Awaka, J., Le, M., et al. (2017). *GPM/DPR Level–2 algorithm theoretical basis document. NASA/JAXA Technical Report*. Retrieved from https://pps.gsfc.nasa.gov/Documents/ATBD_DPR_201811_with_Appendix3b.pdf

Jones, C. (2019). Recent changes in the South America low-level jet. *Climate and Atmospheric Science*, *2*(1), 1–8. https://doi.org/10.1038/s41612-019-0077-5

Junquas, C., Takahashi, K., Condom, T., Espinoza, J. C., Chávez, S., Sicart, J. E., & Lebel, T. (2018). Understanding the influence of orography on the precipitation diurnal cycle and the associated atmospheric processes in the central Andes. *Climate Dynamics*, *50*(11–12), 3995–4017. https://doi.org/10.1007/s00382-017-3858-8

Killeen, T. J., Douglas, M., Consiglio, T., Jørgensen, P. M., & Mejia, J. (2007). Dry spots and wet spots in the Andean hotspot. *Journal of Biogeography*, *34*(8), 1357–1373. https://doi.org/10.1111/j.1365-2699.2006.01682.x

Kozu, T., Iguchi, T., Shimomai, T., & Kashiwagi, N. (2009). Raindrop size distribution modeling from a statistical rain parameter relation and its application to the TRMM precipitation radar rain retrieval algorithm. *Journal of Applied Meteorology and Climatology*, *48*(4), 716–724. https://doi.org/10.1175/2008JAMC1998.1

Kubota, T., Iguchi, T., Kojima, M., Liao, L., Masaki, T., Hanado, H., et al. (2016). Statistical method for reducing sidelobe clutter for the Ku-band precipitation radar onboard the GPM Core Observatory. *Journal of Atmospheric and Oceanic Technology*, *43*, 1413–1428. https://doi.org/10.1175/JTECH-D-15-0202.1

Lavado-Casimiro, W., & Espinoza, J. C. (2014). Impact of El Niño and La Niña on rainfall in Peru. *Revista Brasileira de Meteorologia*, *29*, 171–182.

Lavado Casimiro, W. S., Silvestre, E., & Pulache, W. (2010). Tendencias en los extremos de lluvias cerca a la ciudad del Cusco y su relación con las inundaciones de Enero del 2010. Extreme rainfall trends around Cusco and its relationship with the floods in January. *Revista Peruana Geo-Atmosférica*, *2*, 89–98.

L'Heureux, M. L., Takahashi, K., Watkins, A. B., Barnston, A. G., Becker, E. J., Di Liberto, T. E., et al. (2017). Observing and predicting the 2015/16 El Niño. *Bulletin of the American Meteorological Society*, *98*(7), 1363–1382. https://doi.org/10.1175/BAMS-D-16-0009.1

Liao, L., & Meneghini, R. (2019). A modified dual-wavelength technique for Ku-and Ka-band radar rain retrieval. *Journal of Applied Meteorology and Climatology*, *58*(1), 3–18. https://doi.org/10.1175/JAMC-D-18-0037.1

Liu, C. (2011). Rainfall contributions from precipitation systems with different sizes, convective intensities, and durations over the tropics and subtropics. *Journal of Hydrometeorology*, *12*(3), 394–412. https://doi.org/10.1175/2010JHM1320.1

Liu, C., Zipser, E. J., Cecil, D. J., Nesbitt, S. W., & Sherwood, S. (2008). A cloud and precipitation feature database from nine years of TRMM observations. *Journal of Applied Meteorology and Climatology*, *47*(10), 2712–2728. https://doi.org/10.1175/2008JAMC1890.1

Lowman, L. E., & Barros, A. P. (2014). Investigating links between climate and orography in the central Andes: Coupling erosion and precipitation using a physical-statistical model. *Journal of Geophysical Research: Earth Surface*, *119*, 1322–1353. https://doi.org/10.1002/2013JF002940

Marengo, J. A., Soares, W. R., Saulo, C., & Nicolini, M. (2004). Climatology of the low-level jet east of the Andes as derived from the NCEP-NCAR reanalyses: Characteristics and temporal variability. *Journal of Climate*, *17*(12), 2261–2280. https://doi.org/10.1175/1520-0442(2004)017%3C2261:COTLJE%3E2.0.CO;2

Martínez-Castro, D., Kumar, S., Flores Rojas, J. L., Moya-Álvarez, A., Valdivia-Prado, J. M., Villalobos-Puma, E., et al. (2019). The impact of microphysics parameterization in the simulation of two convective rainfall events over the Central Andes of Peru using WRF-ARW. *Atmosphere*, *10*(8), 442. https://doi.org/10.3390/atmos10080442

Menne, M. J., Durre, I., Vose, R. S., Gleason, B. E., & Houston, T. G. (2012). An overview of the global historical climatology network-daily database. *Journal of Atmospheric and Oceanic Technology*, *29*(7), 897–910. https://doi.org/10.1175/JTECH-D-11-00103.1

Mohr, K. I., Slayback, D., & Yager, K. (2014). Characteristics of precipitation features and annual rainfall during the TRMM era in the Central Andes. *Journal of Climate*, *27*(11), 3982–4001. https://doi.org/10.1175/JCLI-D-13-00592.1

Montini, T. L., Jones, C., & Carvalho, L. M. (2019). The South American low-level jet: a new climatology, variability, and changes. *Journal of Geophysical Research: Atmospheres*, *124*, 1200–1218. https://doi.org/10.1029/2018JD029634

Moya-Álvarez, A., Gálvez, J., Holguín, A., Estevan, R., Kumar, S., Villalobos, E., et al. (2018). Extreme rainfall forecast with the WRF-ARW model in the Central Andes of Peru. *Atmosphere*, *9*(9), 362. https://doi.org/10.3390/atmos9090362

Myers, N., Mittermeier, R. A., Mittermeier, C. G., Da Fonseca, G. A., & Kent, J. (2000). Biodiversity hotspots for conservation priorities. *Nature*, *403*(6772), 853–858. https://doi.org/10.1038/35002501

Nesbitt, S. W., & Anders, A. M. (2009). Very high resolution precipitation climatologies from the Tropical Rainfall Measuring Mission precipitation radar. *Geophysical Research Letters*, *36*, L15815. https://doi.org/10.1029/2009GL038026

Perry, L. B., Seimon, A., Andrade-Flores, M. F., Endries, J. L., Yuter, S. E., Velarde, F., et al. (2017). Characteristics of precipitating storms in glacierized tropical Andean cordilleras of Peru and Bolivia. *Annals of the American Association of Geographers*, *107*(2), 309–322. https://doi.org/10.1080/24694452.2016.1260439

Peterson, T. C., & Vose, R. S. (1997). An overview of the Global Historical Climatology Network temperature database. *Bulletin of the American Meteorological Society*, *78*(12), 2837–2849. https://doi.org/10.1175/1520-0477(1997)078%3C2837:AOOTGH%3E2.0.CO;2

Rabatel, A., Francou, B., Soruco, A., Gomez, J., Ceballos, J. L., Basantes, R., et al. (2017). Current state of glaciers in the tropical Andes: A multi-century perspective on glacier evolution and climate change. *The Cryosphere*, *7*. https://doi.org/10.5194/tc-7-81-2013

Ramírez, I. J., & Briones, F. (2017). Understanding the El Niño costero of 2017: The definition problem and challenges of climate forecasting and disaster responses. *International Journal of Disaster Risk Science*, *8*(4), 489–492.

Rasmussen, K. L., Chaplin, M. M., Zuluaga, M. D., & Houze, R. A. Jr. (2016). Contribution of extreme convective storms to rainfall in South America. *Journal of Hydrometeorology*, *17*(1), 353–367. https://doi.org/10.1175/JHM-D-15-0067.1

Rasmusson, E. M., & Carpenter, T. H. (1982). Variations in tropical sea surface temperature and surface wind fields associated with the Southern Oscillation/El Niño. *Monthly Weather Review*, *110*(5), 354–384. https://doi.org/10.1175/1520-0493(1982)110%3C0354:VITSST%3E2.0.CO;2

Regard, V., Lagnous, R., Espurt, N., Darrozes, J., Baby, P., Roddaz, M., et al. (2009). Geomorphic evidence for recent uplift of the Fitzcarrald Arch (Peru): A response to the Nazca Ridge subduction. *Geomorphology*, *107*(3–4), 107–117. https://doi.org/10.1016/j.geomorph.2008.12.003

Romatschke, U., & Houze, R. A. Jr. (2013). Characteristics of precipitating convective systems accounting for the summer rainfall of tropical and subtropical South America. *Journal of Hydrometeorology*, *14*(1), 25–46.

Romatschke, U., & Houze, R. A. Jr. (2010). Extreme summer convection in South America. *Journal of Climate*, *23*(14), 3761–3791. https://doi.org/10.1175/2010JCLI3465.1

Saavedra, M., & Takahashi, K. (2017). Physical controls on frost events in the central Andes of Peru using in situ observations and energy flux models. *Agricultural and Forest Meteorology*, *239*, 58–70. https://doi.org/10.1016/j.agrformet.2017.02.019

Salio, P., Nicolini, M., & Saulo, A. C. (2002). Chaco low-level jet events characterization during the austral summer season. *Journal of Geophysical Research*, *107*(D24), 4816. https://doi.org/10.1029/2001JD001315

Stein, A. F., Draxler, R. R., Rolph, G. D., Stunder, B. J., Cohen, M. D., & Ngan, F. (2015). NOAA's HYSPLIT atmospheric transport and dispersion modeling system. *Bulletin of the American Meteorological Society*, *96*(12), 2059–2077. https://doi.org/10.1175/BAMS-D-14-00110.1

Sulca, J., Takahashi, K., Espinoza, J. C., Vuille, M., & Lavado-Casimiro, W. (2018). Impacts of different ENSO flavors and tropical Pacific convection variability (ITCZ, SPCZ) on austral summer rainfall in South America, with a focus on Peru. *International Journal of Climatology*, *38*(1), 420–435.

Sun, X., & Barros, A. P. (2015a). Impact of Amazonian evapotranspiration on moisture transport and convection along the eastern flanks of the tropical Andes. *Quarterly Journal of the Royal Meteorological Society*, *141*(693), 3325–3343. https://doi.org/10.1002/qj.2615

Sun, X., & Barros, A. P. (2015b). Isolating the role of surface evapotranspiration on moist convection along the eastern flanks of the tropical Andes using a quasi-idealized approach. *Journal of the Atmospheric Sciences*, *72*(1), 243–261. https://doi.org/10.1175/JAS-D-14-0048.1

Takahashi, K., & Martínez, A. G. (2019). The very strong coastal El Niño in 1925 in the far-eastern Pacific. *Climate Dynamics*, *52*(12), 7389–7415. https://doi.org/10.1007/s00382-017-3702-1

Takahashi, K., Montecinos, A., Goubanova, K., & Dewitte, B. (2011). ENSO regimes: Reinterpreting the canonical and Modoki El Niño. *Geophysical Research Letters*, *38*, L10704. https://doi.org/10.1029/2011GL047364

Testik, F. Y., Barros, A. P., & Bliven, L. F. (2006). Field observations of multimode raindrop oscillations by high-speed imaging. *Journal of the Atmospheric Sciences*, *63*(10), 2663–2668.

Tokay, A., Wolff, D. B., & Petersen, W. A. (2014). Evaluation of the new version of the laser-optical disdrometer, OTT Parsivel2. *Journal of Atmospheric and Oceanic Technology*, *31*(6), 1276–1288. https://doi.org/10.1175/JTECH-D-13-00174.1

Vera, C., Baez, J., Douglas, M., Emmanuel, C. B., Marengo, J., Meitin, J., et al. (2006). The South American low-level jet experiment. *Bulletin of the American Meteorological Society*, *87*(1), 63–78. https://doi.org/10.1175/BAMS-87-1-63

Vuille, M., Francou, B., Wagnon, P., Juen, I., Kaser, G., Mark, B. G., & Bradley, R. S. (2008). Climate change and tropical Andean glaciers: Past, present and future. *Earth-Science Reviews*, *89*, 79–96. https://doi.org/10.1016/j.earscirev.2008.04.002

Wilson, A. M., & Barros, A. P. (2014). An investigation of warm rainfall microphysics in the southern Appalachians: Orographic enhancement via low-level seeder-feeder interactions. *Journal of the Atmospheric Sciences*, *71*(5), 1783–1805. https://doi.org/10.1175/JAS-D-13-0228.1

Wilson, A. M., & Barros, A. P. (2015). Landform controls on low level moisture convergence and the diurnal cycle of warm season orographic rainfall in the Southern Appalachians. *Journal of Hydrology*, *531*, 475–493. https://doi.org/10.1016/j.jhydrol.2015.10.068

Zubieta, R., Saavedra, M., Silva, Y., & Giráldez, L. (2017). Spatial analysis and temporal trends of daily precipitation concentration in the Mantaro River basin: Central Andes of Peru. *Stochastic Environmental Research and Risk Assessment*, *31*(6), 1305–1318. https://doi.org/10.1007/s00477-016-1235-5